Investigation of aerodynamics, wake dynamics, and aeroacoustic characteristics of a full-configuration tiltrotor aircraft during transition flight

Sang Min Son (손상민), Chan-Ho Song (송찬호), M. Sadegh Araghizadeh, Rho Shin Myong (명노신), Hakjin Lee[a] (이학진)

School of Aerospace Engineering, Gyeongsang National University, Jinju, Gyeongnam 52828, South Korea

[a)]Author to whom correspondence should be addressed: hlee@gnu.ac.kr

Abstract

This study presents a numerical analysis of the aerodynamic and aeroacoustic behavior of a full-configuration tiltrotor aircraft during transition flight. This regime poses unique challenges due to the combined effects of varying nacelle tilt angles, rotor–fuselage aerodynamic interference, and complex unsteady wake interactions. Herein, the XV-15 tiltrotor configuration is analyzed using a coupled-vortex framework that incorporates a source-doublet panel method and time-accurate vortex particle method, enabling accurate predictions of unsteady aerodynamic loads and wake development. Rotor noise is evaluated using Farassat's Formulation 1A of the Ffowcs Williams–Hawkings equation, focusing on tonal noise radiation associated with unsteady blade loading. Results indicate that increasing the nacelle tilt angle results in stronger aerodynamic asymmetry, intensifying unsteady blade loads and generating highly distorted wake structures. The developed helical wake transitions into a more irregular, turbulent wake as the nacelles approach the helicopter mode, directly affecting rotor performance and noise radiation. Moreover, fuselage and wing substantially alter wake development, enhances wake interactions, and contributes to additional loading noise components. Aeroacoustic analysis revealed that the overall sound-pressure level increased by ~4 dB as the nacelle tilt angle varied from 15° to 60°, accompanied by a forward shift in dominant noise lobes. Notably, phase differences in sound pressure emitted from the rotor blades induce constructive and destructive interferences depending on observer location. These findings contribute to advancing the understanding of transition flight aerodynamics and aeroacoustics, with implications for next-generation rotorcraft.

1. Introduction

Recent advances in rotorcraft technology, including next-generation helicopters and urban air mobility (UAM) systems, have spurred interest in advanced propulsion architectures, such as tiltrotors, coaxial rotors, and multirotor configurations. Tiltrotor aircraft combine the vertical takeoff and landing capabilities of helicopters with the high-speed cruise efficiency of fixed-wing aircraft. The development of tiltrotor technology dates back to the 1950s, beginning with the National Aeronautics and Space Administration (NASA) Bell XV-3 program [1], followed by successful flight demonstrations of the XV-15 tiltrotor aircraft in the 1970s and 1980s [2]. The V-22 Osprey [3], the first operational military tiltrotor, remains in active service. Meanwhile, the more recent Bell V-280 Valor was selected for the U.S. Army's Future Long-Range Assault Aircraft program [4]. UAM platforms employing tiltrotor configurations, such as Joby Aviation's S4, Archer's Midnight, and Supernal's S-A2, are being developed, highlighting the increasing potential of tiltrotor systems for civilian and military applications.

Tiltrotor aircraft exhibit unique and highly complex aerodynamic characteristics, particularly during transition flight. Their propulsion system features large-diameter rotors mounted on rotating nacelles at the wingtips, which enables varying nacelle tilt angles during flight. During transition flight, the aircraft experiences rapid changes in flight speed, blade pitch angle, and inflow conditions as the nacelles rotate between helicopter and airplane modes. These variations induce substantial changes in the effective angle of attack and inflow velocity distribution across the rotor disk, often leading to highly nonlinear aerodynamic phenomena, such as strong blade–vortex interactions (BVIs), unsteady rotor–fuselage or rotor–wing interference, and severe wake interactions [5–8], which can considerably affect rotor performance, dynamic stability, and acoustic emissions [9,10]. Capturing the unsteady rotor aerodynamics and wake dynamics of tiltrotor aircraft enables accurate predictions of their aerodynamic performance and noise characteristics.

The inherently unsteady and asymmetric flow environment encountered during transition flight distinguishes the aerodynamics of tiltrotors from those of helicopters and fixed-wing aircraft. This regime is characterized by varying inflow conditions and strong aerodynamic interference among key components, including rotor–rotor, rotor–fuselage, and rotor–wing interactions. These effects directly influence rotor performance, structural loading, and noise generation. Therefore, accurate predictions of interactional aerodynamics and mutual wake interference in full-configuration tiltrotor systems are essential. Zanotti et al. [11,12] investigated the aerodynamic performance and wake behavior of the XV-15 tiltrotor aircraft operating in different flight modes,

identifying asymmetric blade loading and strong wake interactions. Garcia and Barakos [13] conducted high-fidelity computational fluid dynamics (CFD) simulations of the ERICA tiltrotor, highlighting significant rotor–wing interference effects and pressure variations on the fuselage and wing surfaces during transition flight. Zhenlong et al. [14] investigated rotor–wing interaction phenomena on the V-22 tiltrotor aircraft, demonstrating that the wing experiences amplified lift and pitching moments when exposed to unsteady rotor wake during transition flight. Droandi et al. [15,16] analyzed the effects of nacelle and tilting wing angles on the aerodynamic performance of the rotor thrust and propulsive force of a tiltwing aircraft through experiments and CFD simulations, highlighting the importance of appropriate attitude control for improving aircraft performance during transition and forward flight. Felker and Light [17] explored the effects of geometric variations, including rotor–wing distance, wing incidence, flap angle, and rotating direction, on the aerodynamic performance of rotor and wing. Lim [18] examined the impact of rotor downwash on the aerodynamic performance of a simplified XV-15 tiltrotor configuration during high-speed forward flight through high-fidelity computational simulations. Appleton et al. [19] reported significant aerodynamic interference between rotor wake and tail surfaces, which affect aircraft trim and stability during tilt maneuvers. These reports underscore the need for high-resolution modeling of unsteady inflow and wake-induced loads using full-configuration aircraft. Tugnoli et al. [20] employed the mid-fidelity solver DUST to investigate the influence of rotor–wing interactions and wake diffusion on the vortex shedding, lift, and power requirements of tiltwing electric vertical takeoff and landing (eVTOL) aircraft in airplane and helicopter modes.

In addition to aerodynamic complexity, rotor noise is a critical consideration in tiltrotor operations, particularly during transition flight, where inflow asymmetry, azimuthal variation in aerodynamic loading, and wake interactions result in pronounced acoustic emissions. Noise radiation in this regime is of particular concern for military applications, where acoustic detectability affects survivability, and for civil urban operations, where noise exposure limits public acceptance. During flight testing of the XV-15, Edward [21] reported significant changes in noise directivity and amplitude associated with nacelle tilt angle during horizontal, climb, and descent maneuvers. Conner et al. [22,23] demonstrated that optimizing the nacelle tilt and approach angle profiles based on operational parameters, such as flight speed and altitude, can reduce the sound exposure level by up to 7 dB, underscoring the acoustic sensitivity of the transition regime. Other researchers have investigated the underlying flow mechanisms that contribute to noise radiation. Bao et al. [24] examined rotor–fuselage interactions, including the fountain effect during hovering, reporting a strong correlation between induced flow

structures and rotor noise levels. Jamaluddin et al. [25] analyzed the aerodynamic and acoustic characteristics of a tiltrotor platform as a function of nacelle tilt angle, revealing that changes in turbulent kinetic energy and inflow structure can significantly affect the overall sound-pressure level (OASPL). Coelho [26] studied rotor–rotor interactions in a tiltrotor UAM configuration and reported that the downstream rotor wake at high nacelle tilt angles can induce considerable acoustic interference and amplification. Sagaga and Lee [27,28] compared isolated and full-configuration rotors on a side-by-side eVTOL platform during hovering, demonstrating that aerodynamic interference increases with increasing rotor overlap, leading to an increase in OASPL. Jia and Lee [29,30] conducted high-fidelity CFD and acoustic simulations on one- and six-passenger quadrotor UAM aircraft and identified self-BVIs as the primary noise source. Furthermore, they found that overlapping the rotor and fuselage in a side-by-side rotor configuration directly affected noise generation, with a 25% overlap yielding the most effective noise mitigation. Smith et al. [31] reported that aerodynamic interactions between the wing and rotor significantly alter loading noise characteristics owing to asymmetric load distribution on the rotor blade. Kim et al. [32] conducted high-fidelity CFD simulations to investigate mutual aerodynamic and acoustic interactions between the rotor and airframe, revealing that the presence of the airframe increases unsteady loading on the rotor blades and enhances aerodynamic load fluctuations owing to a partial ground effect.

Table I summarizes recent studies on tiltrotor aircraft. As previously discussed, unsteady flow during transition flight and aerodynamic interactions between aircraft components are unique features of the tiltrotor system and important factors in determining the aerodynamic and aeroacoustic performance of tiltrotor aircraft. Various computational and experimental studies have explored tiltrotor aerodynamics and acoustics; however, most have been limited to steady-state flight modes, such as hover or cruise maneuvers, or have employed simplified configurations that do not fully capture the intrinsic complexity of transition flight. By contrast, the transition-flight regime, characterized by a misalignment between the rotor axis and flight direction, introduces a fundamentally unsteady aerodynamic environment. Moreover, detailed exploration of asymmetric aerodynamic behavior, unsteady wake evolution, and interactional phenomena under varying nacelle tilt angles remains limited. In particular, the complex wake dynamics of the tiltrotor system due to simultaneous rotor–rotor, rotor–fuselage, and rotor–wing interactions have not been thoroughly analyzed in full-configuration systems. Additionally, to our knowledge, studies exploring the effects of nacelle tilt angle on noise propagation in a full-configuration tiltrotor aircraft remain relatively scarce. Spatial and temporal distortions of the wake

structure alter the effective inflow to the rotor blades and induce fluctuating aerodynamic loads, which serve as the primary source of rotor noise and play a pivotal role in shaping the acoustic footprint. Therefore, time-dependent simulations of wake evolution during transition flight are required to accurately predict unsteady aerodynamic loads acting on the rotors and fuselage as well as the resulting rotor noise levels.

Table I. Detailed review of aerodynamic and aeroacoustic analysis of tiltrotor aircraft

Paper Details	Model	Research Details
Jamaluddin et al. [25] (2024)	Isolated rotor	Experimental investigation of noise characteristics of an isolated tiltrotor under varying tilt angles
Lim [18] (2021)	Rotor–wing	High-fidelity CFD analysis of rotor–wing interactions in tiltrotor aircraft during cruise flight
Bao et al. [24] (2023)	Full configuration	Analysis of rotor–fuselage interaction effects on aerodynamic and acoustic characteristics of a tiltrotor during hovering flight
Zanotti et al. [33] (2021)	Full configuration	Mid-fidelity numerical analysis of aerodynamic performance and flow physics of a tiltrotor aircraft
Present study	Full configuration	Comprehensive investigation of tilt angle effects on aerodynamic loads, wake evolution, and noise radiation of tiltrotor aircraft

To address these knowledge gaps, this study comprehensively analyzed the aerodynamics, wake dynamics, and aeroacoustics of a full-configuration tiltrotor aircraft in transition flight. Prior research has provided valuable insights into rotor performance and structural dynamics; nevertheless, few studies have captured unsteady wake dynamics and their impact on rotor–fuselage interference and noise generation. Moreover, most existing computational studies rely either on isolated rotor models or computationally expensive CFD solvers, limiting their applicability in parametric investigations. By contrast, this study employed a mid-fidelity coupled-vortex method that integrated a source-doublet panel method to model the rotor and fuselage and a Lagrangian vortex particle method (VPM) to simulate wake convection, enabling high-resolution preservation of wake deformation. The resulting unsteady aerodynamic loads acting on the rotor blades were utilized as input for noise prediction; further, Farassat's Formulation 1A of the Ffowcs Williams–Hawkings (FW–H) equation was utilized to assess tonal noise, specifically the thickness and dominant loading noise components at different blade pass frequencies (BPFs). The XV-15 tiltrotor configuration was analyzed at four nacelle tilt angles (15°, 30°, 45°, and 60°) to explore the influence of nacelle tilt angle on the aerodynamic loads acting on the rotor

blade and wing, wake structure, flow fields, and far-field noise levels. A comprehensive assessment of these effects provides valuable insights into the complex flow structures and interactional noise mechanisms unique to tiltrotor configurations. This study improves the understanding of transition flight aerodynamics and has implications for noise-mitigation strategies and design optimization for next-generation rotorcraft and UAM systems.

2. Numerical Methods

High-fidelity CFD approaches have been employed to examine detailed flow phenomena; however, their substantial computational cost and setup complexity make them impractical for extensive parametric studies involving full configurations with multiple rotors. To address these limitations, this study implements a mid-fidelity simulation framework based on vortex methods to investigate the effects of nacelle tilt angle on the unsteady flow features and acoustic characteristics of full-configuration tiltrotor aircraft during transition flight. This approach integrates a source-doublet panel method to model the rotor blades and fuselage surfaces, a Lagrangian VPM to model wake evolution and convection, and Farassat's Formulation 1A derived from the FW–H equation for rotor noise prediction. This coupled framework offers several advantages over traditional high-fidelity CFD approaches: (1) it eliminates the need for volumetric meshing; (2) it preserves fine-scale wake structures over long distances with minimal numerical dissipation; (3) it enables rapid parametric studies across varying nacelle tilt angles; and (4) it can capture rotor–wake–fuselage interactions and link them to acoustic responses, elucidating the dominant noise mechanisms and radiation directivity in tiltrotor aircraft.

2.1 Source-doublet panel method

The source-doublet panel method assumes the flow to be inviscid, incompressible, and irrotational; under this condition, the governing continuity equation reduces to Laplace's equation for the velocity potential. The general solution to Laplace's equation is derived using Green's second identity, which represents the flow field in terms of the surface distributions of source (σ) and doublet (μ) singularities. By applying these singularities over surface and wake panels, the velocity potential at any field point can be expressed as an integral equation:

$$\phi^*(x,y,z) = -\frac{1}{4\pi}\oiint_{S_B}[\sigma(\frac{1}{r}) - \mu\nabla(\frac{1}{r})\mathbf{n}]dS + \frac{1}{4\pi}\oiint_{S_W}\mu\nabla(\frac{1}{r})\mathbf{n}dS + \phi_\infty \quad (1)$$

To numerically evaluate the velocity potential, Dirichlet boundary conditions are imposed at each collocation point on the body surface, reducing the integral equation to a system of algebraic equations. This discretized

form enables the representation of flow using panels with constant-strength singularities [34]. For numerical implementation, the body and wake surfaces are discretized into rectilinear panels, comprising N panels on the body surface and N_w panels along the wake. The influence coefficients A_k, C_j, and B_k are computed using the geometric relationships among the discretized source and doublet elements.

The unknown doublet (μ) strength can be computed by solving a system of linear algebraic equations (Eq. (2)), while the source (σ) strength on the rotor and fuselage surface is determined by applying the Neumann boundary condition, as given by Eq. (3):

$$\sum_{k=1}^{N} C_k \mu_k + \sum_{j=1}^{N_W} C_j \mu_{W,j} - \sum_{k=1}^{N} B_k \sigma_k = 0 \quad , \tag{2}$$

$$\sigma_k = -(\mathbf{V}_\infty + \mathbf{V}_{rel} + \Omega \times \mathbf{r}) \cdot \mathbf{n}_k \quad . \tag{3}$$

To account for unsteady flow effects induced by blade motion and wake convection, the time-dependent kinematic velocity is incorporated into the Neumann boundary condition during explicit time-marching simulations. The Neumann boundary condition is employed to determine the source (σ) strength by enforcing zero normal flow conditions. The time-dependent kinematic velocity includes contributions from the freestream velocity, relative translational motion of the blade (e.g., flapping or pitching), and rotational motion of the reference frame; this enables accurate enforcement of the Neumann boundary condition under unsteady flight conditions.

After obtaining the surface μ strength, the wake doublet (μ_w) strength is evaluated by applying the Kutta condition at the trailing edge:

$$\mu_W = \mu_u - \mu_l \quad . \tag{4}$$

The μ_w strength is transferred as the initial circulation input to the VPM, where it defines the initial strength of the shed and trailing wakes and governs the downstream wake evolution of the rotor system.

Following the solution of the potential flow field, the pressure coefficient at each collocation point on the rotor blades and fuselage is evaluated based on the local flow velocity resolved in the body-fixed coordinate system:

$$V_l = -\frac{\partial \mu}{\partial \mathrm{l}}, \; V_m = -\frac{\partial \mu}{\partial \mathrm{m}}, \; V_n = -\sigma \quad . \tag{5}$$

Bernoulli's equation (Eq. (6)) is employed to relate the pressure coefficient to the local velocity magnitude:

$$C_p = 1 - \frac{|\mathbf{V}_{total}|^2}{|\mathbf{V}_{kinenatic}|^2} - \frac{2}{|\mathbf{V}_{kinenatic}|^2}\frac{\partial \phi}{\partial t} \quad . \tag{6}$$

For cases where the freestream Mach number exceeds 0.3, a Prandtl–Glauert compressibility correction is applied to account for compressibility effects. In addition, viscous drag is estimated using airfoil aerodynamic lookup tables, which provide sectional drag coefficients as a function of the local Reynolds number and effective angle of attack based on the evaluated sectional flow conditions.

2.2 VPM

Accurate modeling of rotor wake dynamics is critical for predicting unsteady aerodynamic loading and the resultant noise radiation in tiltrotor aircraft, particularly during transition flight, where complex wake–structure interactions dominate. The rotor wake generated by the blade is modeled using a Lagrangian framework rather than an Eulerian one, enabling a more accurate representation of unsteady wake evolution without the numerical dissipation typically associated with volume grid–based solvers. Among Lagrangian approaches, VPM is particularly suitable for capturing the complex wake dynamics encountered in tiltrotor systems, especially during transition flight, where rotor–rotor, rotor–fuselage, and rotor–wing interactions are prominent. In this study, the near-wake (nascent wake) generated from the trailing edge of the blade is initially represented using discrete vortex panels, comprising shed and trailing vortex filaments, to prevent numerical instability. These panels are discretized into a finite number of individual vortex particles propagating downstream with the local convection velocity. This particle representation allows free deformation of the wake structure in space and time, capturing intricate phenomena such as vortex roll-up, merging, and impingement on fuselage or wing surfaces [35]. Such characteristics make VPM highly effective for resolving the wake–wake, wake–rotor, and wake–fuselage interactions that dominate the aerodynamic and acoustic behaviors of tiltrotor aircraft during transition flight. Accordingly, herein, VPM is tightly coupled with the source-doublet panel method to accurately simulate the generation, convection, and interaction of the rotor wake in full-configuration tiltrotor simulations.

The local convection velocity governing particle propagation is determined by the superposition of four contributing flow components:

$$\mathbf{V}_{conv}(\mathbf{s}_m, t) = \mathbf{V}_{\infty} + \mathbf{V}_{ind.blade} + \mathbf{V}_{ind.filament} + \mathbf{V}_{ind.particle} \quad , \tag{7}$$

where $\mathbf{V}_\infty$ denotes the freestream velocity and $\mathbf{V}_{ind.blade}$, $\mathbf{V}_{ind.filament}$, and $\mathbf{V}_{ind.particle}$ signify the velocity induced by the source-doublet panels, representing the rotor blades, nascent wake panels, and previously released vortex particles, respectively. To simulate wake evolution, an explicit time-marching approach is employed. At each time step, the convection velocity of each vortex particle is calculated according to local flow conditions, and particle positions are updated using the second-order Runge–Kutta integration scheme:

$$\frac{d\mathbf{s}_m}{dt} = \mathbf{V}_{conv}(\mathbf{s}_m, t) \quad . \tag{8}$$

Herein, a slow-starting strategy is employed to prevent the generation of strong initial starting vortices, which can adversely affect overall wake development and introduce unphysical instabilities. The rotor rotational speed is gradually increased from zero to its target value over the first rotor revolution using a sinusoidal ramp-up profile, ensuring the smooth onset of rotor motion and promoting stable wake formation. The simulation uses an azimuthal time step of $\Delta\psi = 3°$, corresponding to one blade rotation per 120 steps, and eight rotor revolutions.

The wake flow field is represented by a set of Lagrangian vortex particles (p) that obtain vector-valued vorticity. The velocity induced at the m-th particle by all other particles ($n = 1, 2, \ldots, p$; $n \neq m$) is computed using the Biot–Savart law:

$$\mathbf{V}_{ind.particles}(\mathbf{x}_m, t) = -\sum_{n=1}^{p} \frac{1}{\sigma_{mn}^3} K(\rho)(\mathbf{x}_m - \mathbf{x}_n) \times \boldsymbol{\alpha}_n \quad , \tag{9}$$

where $\mathbf{x}_m$ denotes the position of the m-th particle, $\boldsymbol{\alpha}_n$ refers to the vector-valued circulation strength of the n-th particle. To avoid singularities in the velocity field, a symmetrized smoothing function with a regularization parameter (σ_{mn}) is applied:

$$\sigma_{mn} = \frac{\sqrt{\sigma_m^2 + \sigma_n^2}}{2} \quad , \tag{10}$$

$$\rho = \frac{|\mathbf{x}_m - \mathbf{x}_n|}{\sigma_{mn}} \quad , \tag{11}$$

where ρ is the nondimensionalized inter-particle distance.

The kernel function K indicates that the regularized Biot–Savart kernel is used to compute the induced velocity field from a vortex particle:

$$K(\rho) = \frac{G(\rho) - \xi(\rho)}{\rho} \quad . \tag{12}$$

K is derived from the Green's function solution for the vector stream function, convolved with a prescribed vorticity distribution. Herein, the vorticity distribution is modeled using a three-dimensional, high-order algebraic smoothing function proposed by Winckelmans and Leonard, ensuring a smooth and finite velocity field near the vortex core [36]. The mathematical formulations are as follows:

$$G(\rho) = \frac{1}{4\pi} \frac{\rho^2 + 3/2}{(\rho^2 + 1)^{3/2}}, \tag{13}$$

$$\xi(\rho) = -\frac{1}{\rho} \frac{d^2}{d\rho^2} [\rho G(\rho)] = \frac{15}{8\pi} \frac{1}{(\rho^2 + 1)^{7/2}}. \tag{14}$$

Owing to the $O(N^2)$ computational complexity associated with pairwise interactions among a large number of vortex particles, parallel computations based on the Message Passing Interface are implemented to efficiently calculate the induced velocities. This parallelization is critical for maintaining computational tractability while resolving the wake–wake interactions that govern the large-scale evolution and deformation of the rotor wake.

2.3 FW–H acoustic analogy

Because of their unique configuration and tilt mechanism, tiltrotor aircraft inherently undergo strong aerodynamic interactions among the rotor, wing, and fuselage, which vary substantially with nacelle tilt angle. These interactions are major contributors to tonal and broadband noise, particularly during transition flight. Therefore, accurately predicting the associated noise radiation as a function of nacelle tilt angle is essential for assessing the operational feasibility of tiltrotor systems in urban and military environments with stringent noise constraints. Rotor noise can be categorized into nondeterministic and deterministic components. Nondeterministic components include turbulence ingestion noise, airfoil self-noise, and broadband noise due to random flow disturbances. By contrast, deterministic sources, including thickness noise, loading noise, BVI noise, and high-speed impulsive noise, are caused by blade rotation and dominate the tonal noise spectrum. Thickness noise results from the flow disturbance induced by rotor blade movement, while loading noise originates from the pressure fluctuations caused by aerodynamic loads acting on blade surfaces. These noise sources exhibit periodic and tonal characteristics, leading to high sound-pressure levels (SPL) at BPF and its harmonics, making them primary contributors to the acoustic signature of the rotor. BVI noise, a subset of loading noise, is generated by the impulsive interaction between a rotor blade and the vortices shed by preceding blades. Given their dominant role in tonal noise radiation, the thickness and loading noise components of

tiltrotor aircraft were predicted herein using an acoustic analogy approach, while broadband and nondeterministic sources were excluded from the scope of the study.

Farassat's Formulation 1A, an analytical solution to the FW–H equation based on impermeable surface boundary conditions, is employed to predict the tonal noise components, namely, thickness and loading noise [37,38]. The sound pressure at the observer location is evaluated using surface integrals defined over the rotor blade geometry, where the thickness and loading noise components are expressed as monopole and dipole sources, respectively. The sound-pressure contributions from thickness (p'_T) and loading (p'_L) noise are given by Eqs. (15)–(17):

$$p'(\mathbf{x},t) = p'_T(\mathbf{x},t) + p'_L(\mathbf{x},t) \quad , \tag{15}$$

$$p'_T(\mathbf{x},t) = \frac{1}{4\pi}\int_{f=0}\left[\frac{\rho_0(\dot{v}_n + v_{\dot{n}})}{r\left|1-M_r\right|^2}\right]_{ret} dS + \frac{1}{4\pi}\int_{f=0}\left[\frac{\rho_0 v_n (r\dot{M}_r + a_0 M_r - a_0 M^2)}{r^2\left|1-M_r\right|^3}\right]_{ret} dS \quad , \tag{16}$$

$$p'_L(\mathbf{x},t) = \frac{1}{4\pi a_0}\int_{f=0}\left[\frac{\dot{l}_r}{r\left|1-M_r\right|^2}\right]_{ret} dS + \frac{1}{4\pi}\int_{f=0}\left[\frac{l_r - l_M}{r^2\left|1-M_r\right|^2}\right]_{ret} dS + \frac{1}{4\pi a_0}\int_{f=0}\left[\frac{l_r\left(r\dot{M}_r + a_0 M_r - a_0 M^2\right)}{r^2\left|1-M_r\right|^3}\right]_{ret} dS \quad , \tag{17}$$

where ρ_0 represents the ambient air density, a_0 denotes the speed of sound, *r* refers to the distance between the source and observer, the subscripts *n* and *r* refer to quantities in the surface-normal and radiation directions, respectively, v_n indicates the local surface velocity in the normal direction, l_r corresponds to the radiation-direction component of the unsteady aerodynamic force per unit area acting on the fluid, and *M* refers to the normalized velocity component in the radiation direction, expressed as the Mach number. Notably, the integrals are evaluated at retarded time τ, which accounts for the time delay between sound emission at the source and its perception by the observer:

$$\tau = t - \frac{r}{a_0} = t - \frac{\left|\mathbf{x}-\mathbf{y}\right|}{a_0} \quad . \tag{18}$$

3. Numerical Validation

3.1 Isolated XV-15 rotor blade

To verify the predictive capability of the developed mid-fidelity aerodynamic–acoustic framework, its three core modules were validated separately: rotor aerodynamics analysis, wake modeling, and noise prediction. This approach has been successfully adopted with well-established accuracy in prior studies, including those on rotor aerodynamic and wake simulations [35,37–40], rotor–rotor interference analysis [41–43], rotor–fuselage interaction [44], and rotor noise prediction [45,46]. Herein, the isolated XV-15 tiltrotor blade geometry was employed across all validation cases to ensure consistency and comparability. First, the rotor aerodynamic module was validated by comparing computed surface pressure distributions, thrust, and torque against high-fidelity CFD benchmarks and experimental measurements. Second, wake dynamics–capturing ability was assessed by comparing the predicted tip vortex trajectories with available reference data. Third, the noise prediction module was verified by benchmarking far-field noise footprints obtained using Farassat's Formulation 1A against experimental data.

Before performing transition flight simulations on the full-configuration tiltrotor, the mid-fidelity framework was validated using available performance data from an isolated XV-15 proprotor during hovering and forward flight. The full-scale XV-15 rotor comprised three blades, each with a radius of 3.81 m (150 in), a reference aspect ratio of 10.71, and a root cutoff at 20% of the radius (Table II). Each blade exhibited a substantial twist angle of −40.25°, and the rotor solidity (σ) was 0.089, achieving a tip Mach number of 0.69 under hover conditions. The blade geometry was discretized using a 30 × 31 panel grid (chordwise × spanwise), with refined meshing near the hub and tip regions (Fig. 1). Table III outlines the spanwise distribution of airfoil sections, demonstrating the progression from NACA 64-935 near the hub to NACA 64-208 at the tip, ensuring optimized aerodynamic performance across radial stations. Sectional aerodynamic coefficients for each rotor blade section were obtained from lookup tables to account for viscous and compressibility effects. The tables employed herein were based on data reported by Acree et al. [47].

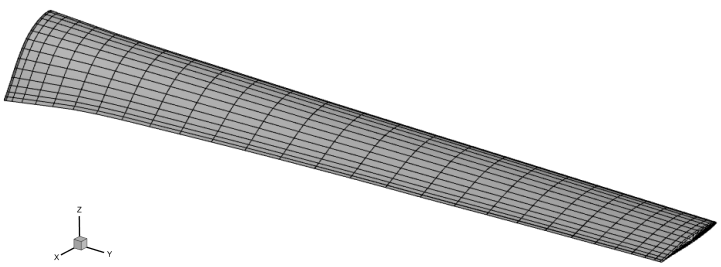

Fig. 1. Geometry and surface discretization of the XV-15 rotor blade modeled using the source-doublet panel method.

Table II. Geometric specifications of the XV-15 rotor blade

Parameter	Value
Number of blades [-]	3
Rotor radius [m]	3.81
Reference aspect ratio [-]	10.71
Root cutoff, R_{cut} [%]	20
Twist angle [°]	−40.25
Rotor solidity, σ [-]	0.089

Table III. Sectional airfoil distribution along the span of the XV-15 rotor blade

r/R	Airfoil
0.09	NACA 64-935
0.17	NACA 64-528
0.51	NACA 64-118
0.80	NACA 64-(1.5)12
1.00	NACA 64-208

3.2 Aerodynamic load validation

This section outlines the validation strategy under hovering and forward flight regimes. For hovering, surface pressure and spanwise thrust distributions were benchmarked against high-fidelity CFD results. For forward flight, integrated thrust and torque coefficients predicted using the vortex methods were compared with CFD results and experimental measurements across a range of collective pitch angles.

The aerodynamic performance during hovering was evaluated using an isolated XV-15 proprotor at a collective pitch angle of 10° with a tip Mach number of 0.69. Fig. 2 presents a comparison of the sectional pressure coefficient (C_p) distributions between the source-doublet panel method and high-fidelity numerical results obtained from Reynolds-averaged Navier–Stokes (RANS) simulations performed using the well-established NASA OVERFLOW2 solver [48,49] at two radial stations along the rotor blade: r/R = 0.83 and 0.94. At r/R = 0.83, the panel method accurately predicted the pressure distribution along the chord, capturing the suction peak near the leading edge and gradual recovery toward the trailing edge, in strong agreement with the CFD results. However, the solver slightly overpredicted the leading-edge suction and underpredicted the pressure recovery on the upper surface at the tip section (r/R = 0.94). These deviations stemmed from the inherent limitations of potential flow formulations in capturing the compressibility effect that becomes

pronounced in high-speed and high-curvature tip regions. Consequently, the predicted pressure distributions exhibited excellent agreement with the RANS CFD results across all radial stations, which was attributed to the application of the Prandtl–Glauert compressibility correction to account for compressibility effects.

To assess the computational efficiency of the present mid-fidelity aerodynamic solver, additional aerodynamic simulations of the XV-15 isolated rotor were carried out using the commercial CFD solver STAR-CCM+ under identical rotor revolutions and simulation conditions. Detached eddy simulation (DES) with k–ω shear stress transport (SST) turbulence model was employed with a time step size of 2°, and the blade surface was discretized with a finest mesh size of 0.8 mm (0.225% of the chord length), resulting in approximately 30 million surface elements. A second-order Roe's flux-difference splitting scheme was applied for inviscid flux evaluation, while viscous terms were computed with a second-order central differencing scheme. Time integration was carried out using an unsteady implicit method with dual-time stepping. Under hovering conditions with collective pitch angles of 5°, 7°, and 10°, the predicted thrust coefficients agreed well with experimental data [50], with an average error of 4.8%. Based on these results, a comparative assessment of computational efficiency was conducted and is summarized in Table II in comparison with reference data [51]. The comparison highlights that, while DES simulations provide accurate predictions, the present mid-fidelity solver achieves similar aerodynamic fidelity with dramatically reduced computational cost, thereby offering a practical and efficient alternative to conventional CFD.

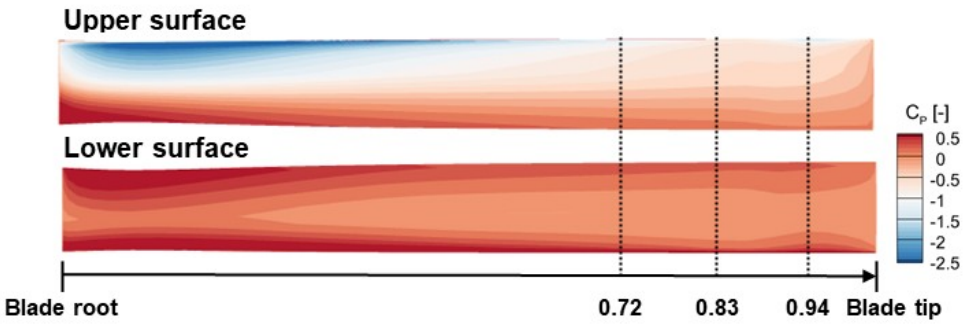

(a)

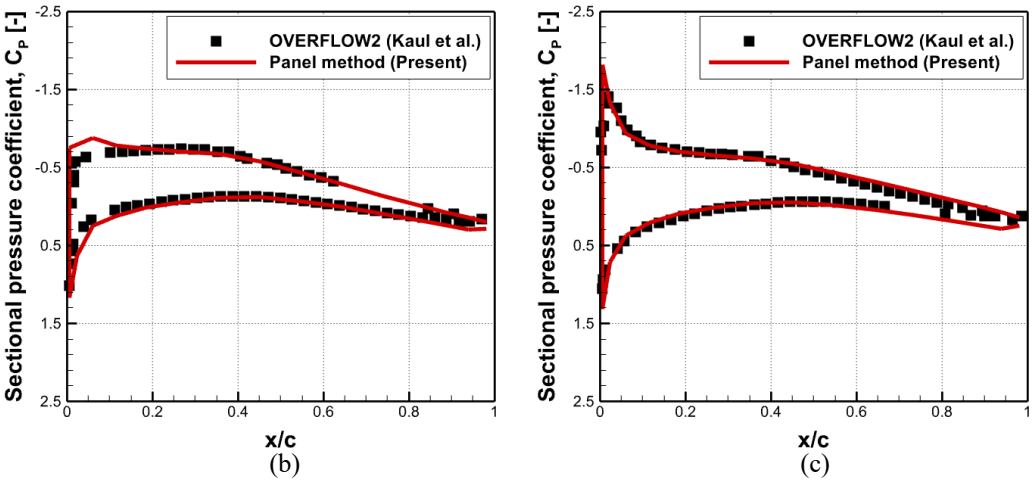

Fig. 2. Comparison of sectional pressure coefficient (C_p) distributions predicted using the source-doublet panel method (red line) and RANS CFD solver OVERFLOW2 (black symbols) at different radial stations: (a) Blade surface pressure contour, (b) r/R = 0.83, and (c) r/R = 0.94. The CFD data were obtained from Kaul et al. [48].

Table IV. Comparison of computing time for aerodynamic calculation of XV-15 isolated rotor in hover

Paper details	Numerical method	Number of CPU	Computing time
Garcia et al. [51]	RANS simulation with $k-\omega$ SST turbulence model	232 cores (Intel Xeon E5620)	17.1 hours (Until convergence)
Present study	DES with $k-\omega$ SST turbulence model	52 cores (Intel Xeon Gold 6230R)	91 hours (10 rev.)
Present study	Panel method with Vortex particle method	52 cores (Intel Xeon Gold 6230R)	1.5 hours (10 rev.)

Fig. 3 presents a comparison of the sectional thrust coefficient (C_T) distributions predicted using the panel method and unsteady RANS-based CFD solver HMB3 reported by Jimenez et al. [51]. The validation was performed under hover conditions at collective pitch angles of 3°, 5°, 10°, and 13° with a tip Mach number of 0.69. The validation presented in Fig. 2 focuses on C_p distributions at different radial locations and fixed pitch angles, while that shown Fig. 3 examines how the spanwise thrust loading varies with increasing blade pitch. The comparison results indicated that the panel method accurately captured the overall trend: the C_T value increased with increasing collective pitch angle, and the predicted distributions agreed well with the CFD results across the entire blade span. A pronounced thrust peak near the blade tip (r/R = 0.9) was consistently observed in both methods. This local amplification was attributed to tip vortex interaction effects, in which the shed vortex from the leading blade induces upwash on the trailing blade, enhancing the local lift and thrust. However, the panel method slightly overpredicted C_T at higher collective pitch settings (particularly at pitch angles of 10° and 13°). This discrepancy was consistent with the surface pressure validation shown in Fig. 2 and was primarily due to the underestimation of compressibility effects near the blade tip at high Mach numbers and loading. Given that thrust is derived from surface pressure integration, overestimation of leading-edge suction directly contributes to integrated thrust predictions. Nevertheless, the solver demonstrated good predictive capability and captured the dominant aerodynamic characteristics relevant to hover performance across a wide range of operating conditions.

The predicted integrated thrust and torque coefficients were compared with experimental and CFD data under airplane-mode conditions to further assess the predictive accuracy of the aerodynamic solver during forward flight. Fig. 4 shows the relationship between the normalized thrust coefficient (C_T/σ) and torque

coefficient (C_Q/σ) at collective pitch angles of 26°, 27°, 28°, and 29°, corresponding to a tip Mach number and an advance ratio of 0.337 and 0.54, respectively. The torque was estimated using an aerodynamic table lookup approach based on sectional airfoil characteristics. Although minor discrepancies were observed over the range of tested conditions, the panel method showed strong agreement with the experimental data published in a NASA technical report [52] and high-fidelity CFD results obtained using the Flow360 solver [53]. Notably, the increasing trend of thrust and torque with higher collective pitch was well captured using the proposed method, and the nearly linear relationship was consistent with the available reference data. The close match across a wide range of blade-loading conditions highlighted the predictive capability of the panel method in computing the integrated aerodynamic performance during forward flight.

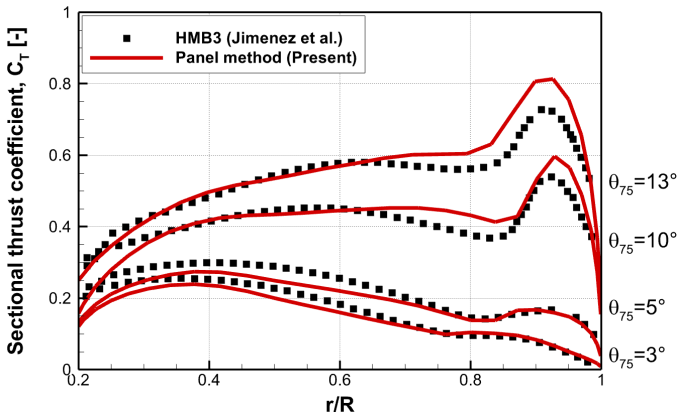

Fig. 3. Comparison of sectional thrust coefficient (C_T) distributions predicted using the source-doublet panel method (red lines) and HMB3 CFD solver (black symbols) at four collective pitch angles: θ_{75} = 3°, 5°, 10°, and 13°. The CFD reference data were obtained from Jimenez et al. [51].

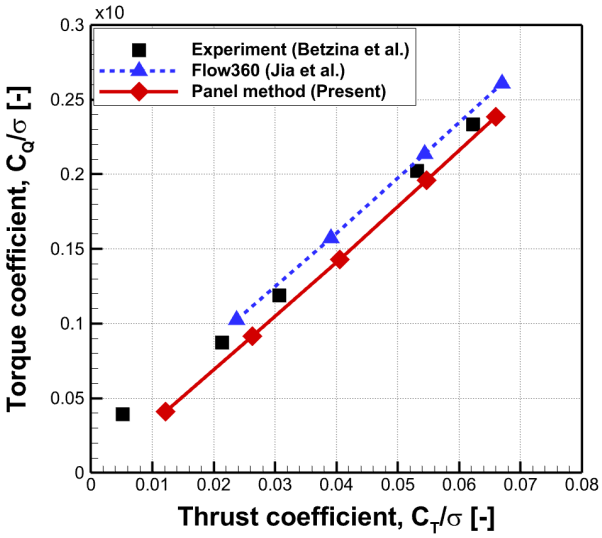

Fig. 4. Comparison of normalized thrust (C_T/σ) and torque (C_Q/σ) coefficients during forward flight at four collective pitch angles: 26°, 27°, 28°, and 29°. Results from the present panel method are compared with experimental data and CFD results reported by Anon et al. [52] and Jia et al. [53], respectively.

3.3 Tip vortex trajectory validation

Accurate prediction of rotor wake dynamics is essential for reliable estimations of aerodynamic and aeroacoustic performance in rotorcraft simulations. In the case of tiltrotor aircraft, this requirement is particularly critical owing to the pronounced interactional phenomena induced by the complex wake structure that evolves with variations in the nacelle tilt angle. These unsteady wake phenomena not only influence blade loading and the induced flow characteristics but also serve as key contributors to noise sources. In this study, VPM was adopted to model rotor wake evolution in near and far fields. This Lagrangian-based method enables the accurate capture of complex wake structures without the numerical dissipation errors typically associated with grid-based Eulerian approaches. The predictive capability of the VPM employed herein was validated in previous studies, including accurate prediction of tip vortex trajectories and wake roll-up behavior in rotor wake modeling [35,37,38,43] and its capability to reproduce induced flow fields [43]. Based on this validated foundation, the present study applied the VPM framework to analyze the wake development of a tiltrotor aircraft during transition flight.

Tip vortices are concentrated vortical structures shed from rotor blade tips that substantially influence aerodynamic interactions among the rotor, fuselage, and wings. Notably, the axial convection and radial contraction of tip vortices determine the effective inflow distribution across the rotor disk and play a decisive role in shaping the far-field wake behavior, particularly in multirotor or tiltrotor configurations. The validation was conducted under isolated hover conditions for the XV-15 proprotor. Simulations were performed at a rotor speed of 589 rpm and a collective pitch angle of 10°, and the resulting wake field was analyzed after 10 rotor revolutions using a time step of 5°. Fig. 5 shows the overall wake structure predicted by VPM, illustrating the coherent helical nature of the tip vortices convecting downstream and exhibiting radial contraction, consistent with classical wake roll-up behavior. For a more quantitative evaluation, Fig. 6 presents the axial convection and radial contraction of the tip vortex cores as a function of wake age extracted from the VPM simulation; further, it presents a comparison with the CFD results obtained from RANS simulations performed with U2NCLE and HELIOS solvers [54,55], incorporating fully turbulent and transition Spalart–Allmaras models, respectively. The VPM predictions at vertical (z/R) and radial (r/R) positions of the tip vortex over the one rotor revolution range matched well with the CFD results. The strong agreement in blade aerodynamic loads and tip vortex trajectories

confirmed the reliability of the coupled panel–VPM framework for predicting rotor aerodynamics and wake dynamics.

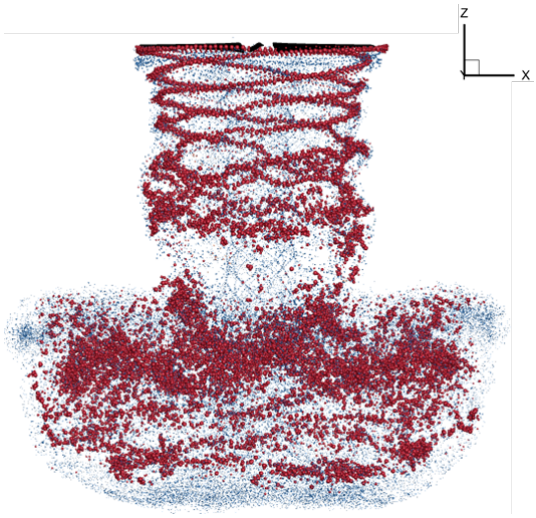

Fig. 5. Wake structure of the isolated XV-15 rotor blade during hovering, visualized using vortex particles after 10 rotor revolutions.

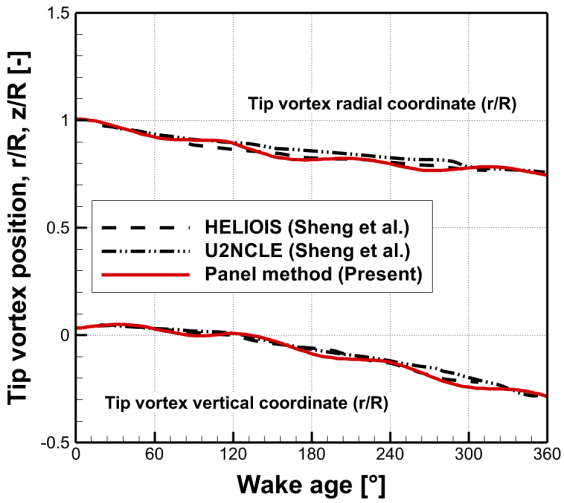

Fig. 6. Comparison of tip vortex core trajectories predicted using the panel–VPM method (solid red line) with CFD results obtained by Sheng et al. [54,55] using U2NCLE and HELIOS solvers.

3.4 Aerodynamic interaction validation

The preceding validation studies have established the reliability of the solver in predicting the aerodynamics and wake evolution of the XV-15 isolated rotor under both hover and forward flight conditions. As highlighted in the Introduction, a unique feature of tiltrotor aircraft is the installation of large rotors at the wingtips with a radius comparable to the wing span. The complex wakes generated by these rotors can strongly influence the aerodynamic performance of the downstream wing and fuselage. Consequently, accurate prediction of rotor–wake–fuselage interactions in full-configuration tiltrotors is essential. The computational framework

employed in this study has already been validated under various models and flight conditions. Bidesh et al. [44] predicted fuselage surface pressures during forward flight of the ROBIN helicopter using tightly coupled CFD and the present solver, demonstrating accurate capture of fuselage–rotor wake interactions. Sadegh et al. [45] confirmed the predictive capability for multi-rotor aircraft by comparing thrust and figure-of-merit results against NASA's side-by-side UAM configurations.

Furthermore, to strengthen confidence in predicting fuselage–rotor wake interactions without relying on CFD coupling, additional validation work was carried out using the ROBIN rotor–fuselage configuration. Simulations were conducted at a rotor speed of 1995 rpm and a collective pitch angle of 12°, with cyclic inputs taken from experimental data. The fuselage geometry is shown in Fig. 7, and unsteady surface pressures at an advance ratio of 0.151 were obtained from the present aerodynamic solver. The pressure histories were extracted at four locations: along the fuselage centerline near the nose (D8), in the mast region where wake interference is strongest (D17), and on both the starboard (D13) and port (D19) sides. The corresponding time histories are presented in Fig. 8. The results show that the four-bladed rotor generates 4/rev periodic oscillations, and the amplitude and phase of the unsteady pressure variations induced by rotor wake interactions are in good agreement with experimental measurements [56] and other computational results [57]. Overall, this validation demonstrates that the solver reliably predicts the variation of surface pressure on fuselage associated with rotor–fuselage interactions.

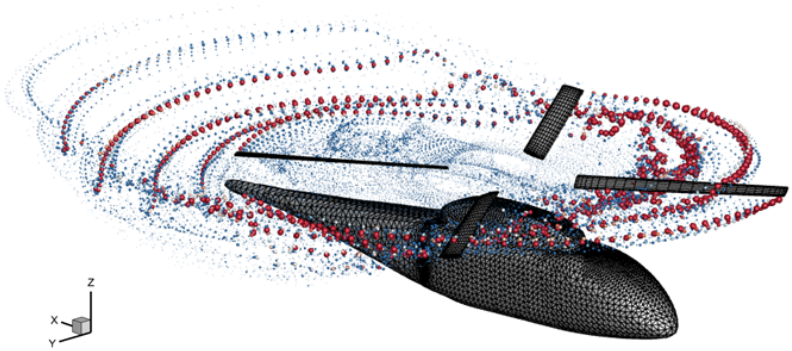

Fig. 7. Source-doublet panel surface grid of the full-configuration ROBIN helicopter model used in the validation, including the fuselage and rotor blades.

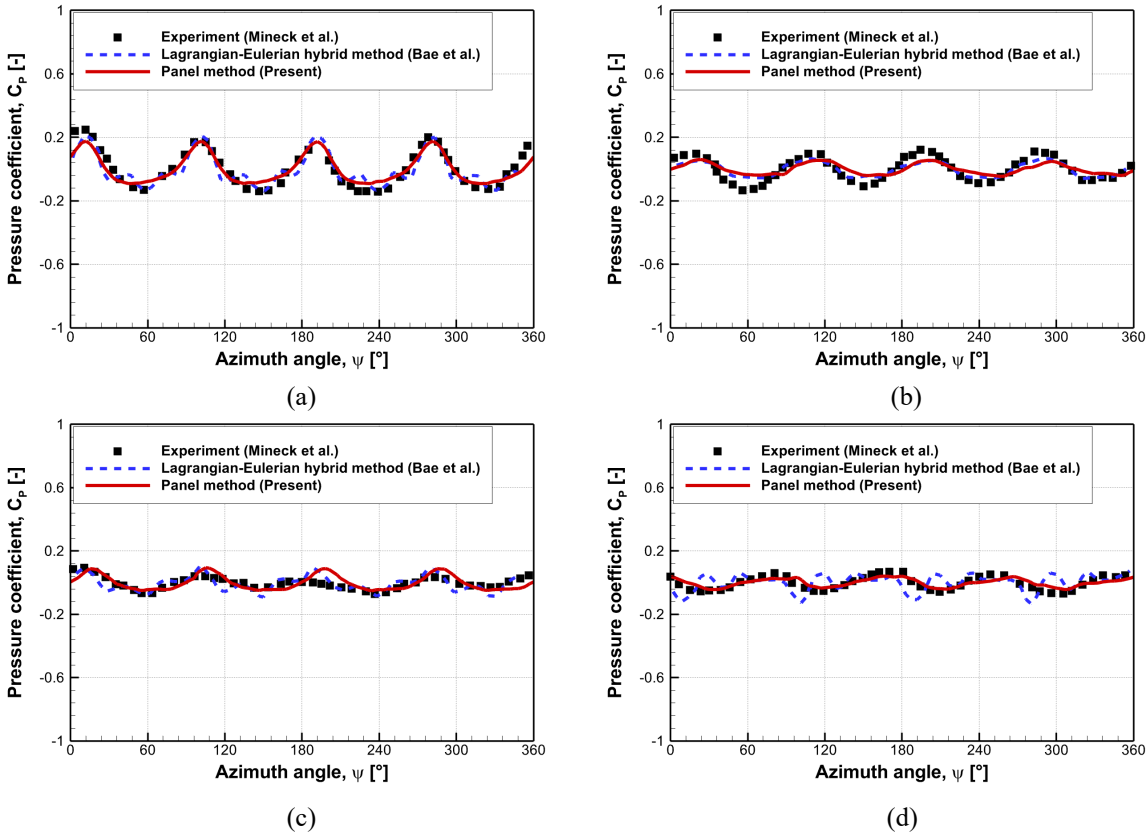

Fig. 8. Unsteady pressures variations on ROBIN fuselage surface at selected points: (a) D8, (b) D13, (c) D17, and (d) D19. Results from the present panel method are compared against experimental data reported by Mineck et al. [56] and reference data reported by Bae et al. [57]

3.5 Noise footprint validation

The acoustic prediction module, based on Farassat's Formulation 1A of the FW–H equation, was validated by comparing the computed noise footprint of the isolated XV-15 proprotor with full-scale experimental measurements. Although the complete tiltrotor configuration was considered herein, only the rotor blade surface was employed as the acoustic source in the noise prediction using the FW–H acoustic analogy. The validation was performed against full-scale experimental data obtained from an XV-15 rotor test conducted in the NASA Ames 80 × 120-foot wind tunnel using the rotor test apparatus [58]. The experiment was designed to capture the BVI noise signature during forward flight. The test conditions included a tip Mach number of 0.691 and an advance ratio of 0.2. The rotor was trimmed to maintain C_T = 0.075, with zero rolling and pitching moments, and the corresponding blade pitch angle was applied in the panel–VPM simulation. The experimental setup included 252 microphones placed 1.8R (where R is the rotor radius) below the rotor disk to measure the sound pressure field. The BVI noise footprint was constructed by integrating SPLs in the frequency range

corresponding to the 10th–50th BPF. Fig. 9 shows the predicted noise footprint at the observer plane, where the circular outline and the rectangular region denote the rotor disk and the experimental microphone array location, respectively. The predicted BVI-SPL distribution exhibited a maximum noise level of 117.3 dB, primarily concentrated between azimuth angles of 90° and 180°, corresponding to the advancing side of the rotor blade. This result agreed with the measured maximum of 121 dB, with a discrepancy of 3.7 dB. This comparison confirms that the noise prediction model, based on loading and thickness sources derived from unsteady aerodynamic loads computed using the coupled panel–VPM solver, offers a reliable and computationally efficient approach for analyzing rotor noise phenomena in tiltrotor aircraft.

Although the proposed framework demonstrated strong agreement with experimental results in the aerodynamic and acoustic validations, several modeling assumptions should be noted. First, the fuselage and wing components were included in the aerodynamic analysis to capture flow interaction effects; however, only the rotor blades were treated as acoustic sources during noise prediction. This simplification neglects scattering and secondary radiation effects that may potentially arise from fuselage and wing surfaces, particularly under complex flow conditions during transition. Second, implementation of the FW–H acoustic analogy assumes impermeable surfaces and excludes quadrupole sources, which may limit its ability to capture broadband noise or flow-induced turbulence effects. To improve prediction accuracy for more complex flight regimes, future studies may consider incorporating permeable FW–H formulations, fuselage scattering models, or hybrid CFD/computational aeroacoustics coupling strategies to capture additional acoustic mechanisms.

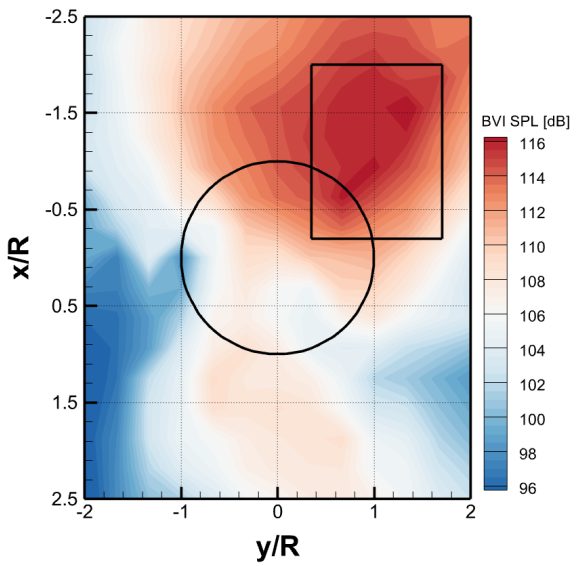

Fig. 9. Predicted BVI noise footprint of the XV-15 rotor during forward flight using Farassat's Formulation 1A. The rotor disk is indicated by the central circle, and the experimental microphone array location is outlined by the black rectangle.

4. Numerical Setup

4.1 XV-15 tiltrotor aircraft and flight conditions

The aircraft configuration used herein was based on the NASA XV-15 tiltrotor, which has served as a benchmark in various rotorcraft studies owing to its well-documented geometry and flight test data. The geometry of the XV-15 tiltrotor aircraft used in the full-configuration simulation included the rotor blades, fuselage, main wing, and tail assembly, while the nacelle was excluded for simplification. Particular attention was given to the aerodynamic modeling of the main wing, as mutual interactions between the rotor and wing surfaces directly affect rotor performance and the magnitude and distribution of downward forces on the wing induced by the rotor wake. The main wing, constructed using a NACA 64A223 airfoil, featured a wingspan of 9.81 m with an aspect ratio of 6.12 and incorporated a sweep angle of 6.5°, a dihedral angle of 2°, and an incidence angle of 5°. The aircraft fuselage had an overall length of 12.83 m. Although high-fidelity control surface deflections were not considered, a refined surface grid was applied to the upper and lower surfaces of wing components to improve the resolution of wake–wing interactions. The key geometric parameters of the XV-15 fuselage and wing are summarized in Table V. The rotor blade geometry, sectional airfoil distribution, and surface discretization were described in Section 3 as part of the validation conducted using the isolated XV-15 rotor blade. The rotor blade was modeled using the source-doublet panel method; its surface grid is shown in Fig. 1 and key parameters are summarized in Tables II and III. Accordingly, the following sections focus on the full-configuration XV-15 aircraft model, including the fuselage and fixed-wing components.

Table V. Geometric specifications of the XV-15 fuselage and wing used in the full-configuration simulation

Parameter	Value
Fuselage length [m]	12.83
Wing span [m]	9.81
Aspect ratio [-]	6.12
Wing airfoil [-]	NACA 64A223
Wing sweep angle [°]	6.5
Wing dihedral angle [°]	2
Wing incidence angle [°]	5

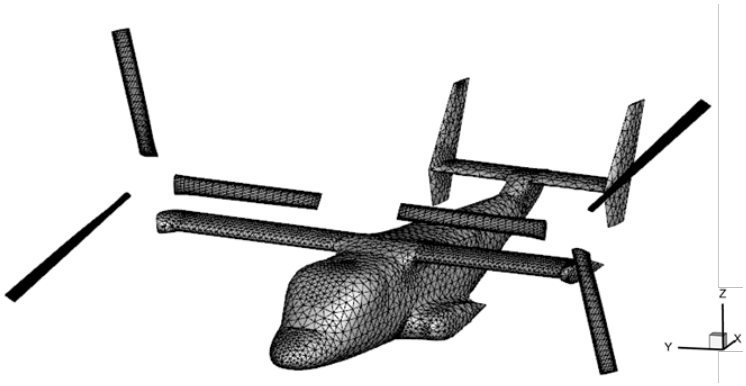

Fig. 10. Source-doublet panel surface grid of the full-configuration XV-15 tiltrotor used in the simulations, including the fuselage, wing, empennage, and rotor blades.

The three-dimensional model included major airframe components, such as the fuselage, main wing, vertical fins, horizontal stabilizers, and rotor blades, for the aerodynamic and aeroacoustic simulations. The full-configuration geometry of the XV-15 tiltrotor aircraft was discretized using the source-doublet panel method (Fig. 10). Rectangular panels were applied to the rotor blades, while triangular panels were used for the fuselage and fixed-wing components. Each rotor blade was discretized with a 30 × 31 panel grid in the chordwise and spanwise directions, with mesh refinement applied near the hub and blade tip, respectively. The remainder of the configuration, including the fuselage, main wing, and tail surfaces, was represented by 8106 triangular panels to balance geometric fidelity with computational efficiency. Panel refinement was applied to regions where strong aerodynamic interactions were expected, such as the rotor–wing junction, to capture wake–airframe interference more accurately. The overall surface grid resolution was sufficient for potential flow analysis within the mid-fidelity framework. To isolate the effects of rotor–wing and rotor–fuselage interactions and reduce model complexity, nacelle components were excluded from the configuration.

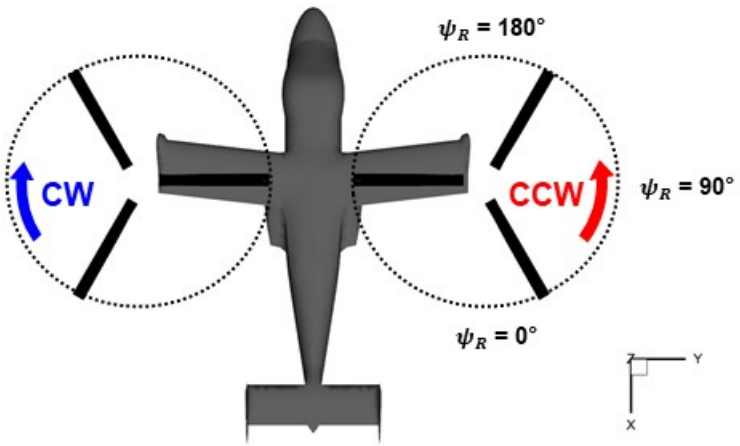

(a)

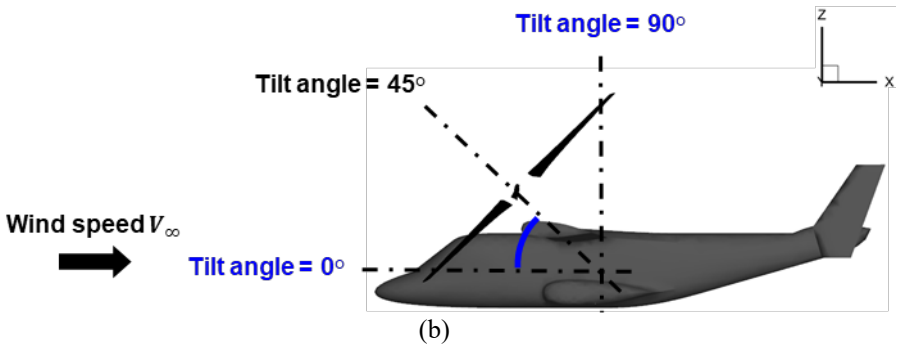

(b)

Fig. 11. (a) Top view of the full-configuration XV-15 tiltrotor showing rotor rotation directions and azimuth angle convention. (b) Side view illustrating the tilt angles.

The rotor system comprised a pair of prop-rotors mounted at the wingtips, with the rotor positions, rotational directions, and azimuth angle conventions shown in Fig. 11(a). The two rotor hubs were laterally separated by 2.6R in the Y-direction, and the rotor blades were positioned 0.38R above the wing surface in the Z-direction, consistent with the full-scale geometry of the XV-15. In the present analysis, only the nacelle tilt angle was varied, with the lateral separation between the rotor hubs maintained throughout all configurations. The port-side rotor rotated in the clockwise direction, while the starboard rotor rotated counterclockwise (CCW) when viewed from above. The azimuth angle (ψ_R) is defined in the rotating frame of the starboard rotor under helicopter-mode conditions, corresponding to a tilt angle of 90° (Fig. 11(b)). ψ_R increases in the CCW direction from the rearward-pointing blade position, with the advancing side of the rotor blade located near the outboard region and the retreating side of the rotor blade located near the inboard region of the main wing. This convention is consistently applied herein to describe blade loading, wake structure, and noise characteristics. The tilt angle is defined as the angle between the rotor axis and the freestream direction, with the freestream aligned along the X-axis in the global coordinate system. A tilt angle of 90° corresponds to the helicopter mode (vertical flight), while a tilt angle of 0° represents the airplane mode (forward flight). Intermediate angles reflect transition states where the rotor axis is progressively reoriented toward the freestream. In this study, representative tilt angles of 15°, 30°, 45°, and 60° were considered to investigate the wake dynamics and aerodynamic and acoustic characteristics of a complete tiltrotor aircraft during transition flight.

For each tilt angle, the freestream velocity, collective pitch angle, and vehicle pitch attitude were varied, while the rotor speed was fixed at 597 rpm to maintain consistency under rotational conditions. The selected flight scenarios were derived from the Generic Tiltrotor (GTR) report by Ferguson and prior studies [7,51,59], ensuring physical relevance. As revealed by Table VI, an increase in the tilt angle led to a reduction in forward

velocity from 65.45 m/s at 15° to 37.17 m/s at 60° and a corresponding decrease in the collective pitch angle from 24.17° to 12.67°. Simultaneously, the vehicle pitch attitude transitioned from −0.27° to 2.85°. Rotor trimming is typically achieved in tiltrotor aircraft through a combination of collective and longitudinal cyclic pitch inputs, along with flap deflections, to satisfy thrust and in-plane force (H-force) requirements. Lateral cyclic pitch was omitted because its control system was not installed on the XV-15 [12,33]. Only collective pitch control was considered in the simulation setup, representing a limitation of the current model. Future studies will incorporate numerical trimming algorithms to determine and apply optimal blade pitch attitudes for each flight condition, reflecting the trim adjustments required to maintain level flight.

Table VI. Simulation conditions for the transition flight of the XV-15 tiltrotor aircraft

Tilt angle [°]	Freestream velocity [m/s]	Collective pitch angle [°]	Rotational speed [rpm]	Vehicle pitch attitude [°]
15	65.45	24.17	597	−0.27
30	56.07	20.33	597	−0.77
45	46.62	16.5	597	1.81
60	37.17	12.67	597	2.85

4.2 Acoustic setup

In this study, aerodynamic predictions using the three-dimensional source-doublet panel method coupled with VPM were combined with aeroacoustic predictions based on Farassat's Formulation 1A of the FW–H equation to predict the noise radiated from tiltrotor blades. The unsteady aerodynamic and wake simulations were conducted using the explicit second-order time-marching scheme with an azimuthal increment of 3° per time step. Each simulation was performed for eight rotor revolutions, with the first rotor revolution employing a smooth ramp-up in rotor speed (Section 2.2) to avoid the instability associated with sudden rotation and unphysical starting vortices. All computations were performed using in-house parallelized vortex solvers executed on a Linux-based high-performance computing cluster with Intel® Xeon® Gold 6230R CPUs operating at 2.1 GHz. Each simulation was executed using 64 physical cores and required ~40 h of wall-clock time per flight condition. The computational cost remained tractable owing to the mid-fidelity nature of the vortex method, which avoided volumetric meshing and enabled high-resolution wake tracking with reduced memory overhead.

The aerodynamic loads after eight rotor revolutions were employed as input for the acoustic predictions. Acoustic post-processing was performed using the time-resolved data obtained over the final rotor revolutions, during which the wake structure and aerodynamic loads reached a converged and periodic state. Specifically, the unsteady aerodynamic loads computed on rotor blade surfaces were used as input for predicting loading noise, while blade kinematic motion (i.e., rotational trajectories) served as the source term for evaluating thickness noise, in accordance with Farassat's Formulation 1A. A source time–dominant algorithm was utilized to efficiently calculate observer times from the retarded time of each rotating blade. A linear temporal interpolation scheme was applied to reconstruct the acoustic source terms at uniform time intervals to enable spectral analysis, which was essential for resolving tonal components such as BPF and its harmonics with high fidelity. The rotational speed of the rotor was fixed at 597 rpm; with three blades per rotor, the resulting BPF was 29.85 Hz. The frequency-domain SPL was computed from the fast Fourier transform of the pressure-time histories recorded at the observer location, and the resulting root-mean-square pressure values were converted to the decibel scale to generate SPL contours. The Hanning window function was applied to mitigate spectral leakage during acoustic signal processing, and a 50% overlap was introduced to enhance frequency resolution.

The noise footprint was computed using a ground-based microphone array to evaluate the noise radiation characteristics during transition flight. As shown in Fig. 12, the observer plane was positioned at 10R (38.2 m) directly below the rotor plane to capture the far-field sound pressure. The array comprised 600 microphones arranged on a rectilinear grid, with 30 points in the X-direction (aligned with the freestream) and 20 points in the Y-direction (aligned with the aircraft wingspan), symmetrically centered about the center of aircraft. The spacing was chosen to resolve tonal directivity patterns and localized noise intensities associated with unsteady loading. The noise radiated from the tiltrotor to each microphone was analyzed to evaluate the contribution of individual noise sources as a function of the tilt angle. This analysis enabled a detailed examination of noise directivity during tiltrotor transition flight.

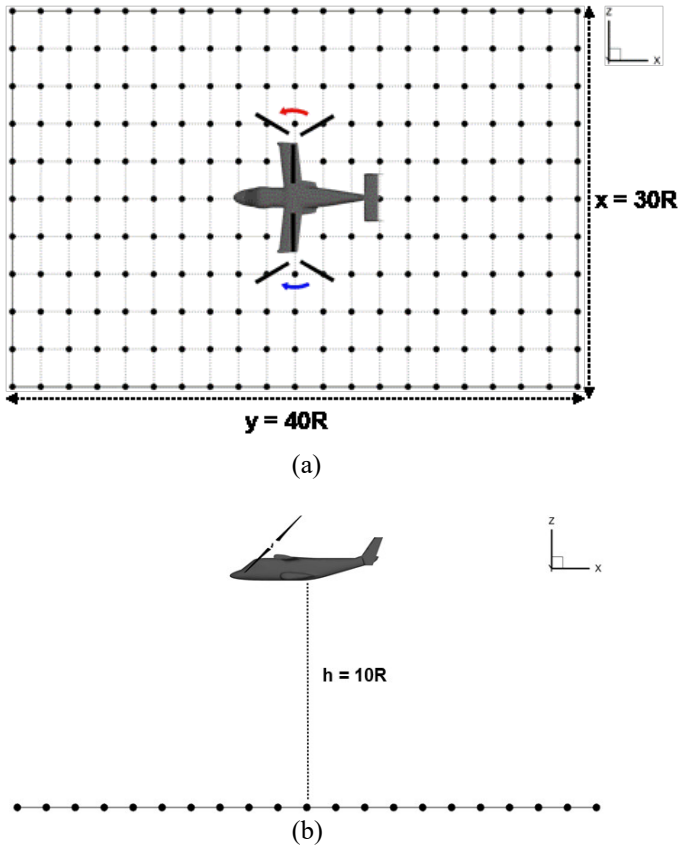

Fig. 12. Microphone array configuration for far-field acoustic analysis (not drawn to scale): (a) Top view and (b) side view.

5. Results and Discussion

5.1 Effects of tilt angle on aerodynamic loading

Fig. 13 presents the C_T time histories for the rotor located on the starboard side at the four tilt angles, and Fig. 14 presents the corresponding C_Q responses. The results were extracted over the last five rotor revolutions to ensure fully developed wake conditions. As shown in Fig. 13, the C_T values exhibit periodic oscillations, with a distinct 3/rev frequency across all tilt angles. This periodicity arises from the three-bladed rotor configuration and reflects the inherent BPF during forward flight. Two notable trends emerge in the C_T response as the tilt angle increases from 15° (near-forward flight) to 60° (near-hovering): (1) the mean thrust increases with increasing tilt angle, attributable to the reduction in the freestream inflow component normal to the rotor disk, thereby increasing the effective angle of attack and enhancing thrust generation; and (2) the thrust oscillation amplitude increases with increasing tilt angle, indicating stronger unsteady aerodynamic effects during the transition toward higher tilt angles. By contrast, C_Q displays a more complex behavior (Fig. 14). Although the

C_Q values also exhibit 3/rev oscillations due to the blade-passing effects, the mean C_Q value decreases with increasing tilt angle. This reduction may be attributed to the combined effects of decreased freestream velocity and parasitic drag during near-hovering, despite the increase in thrust. Furthermore, the torque oscillation amplitude increases with increasing tilt angle, even though the mean torque decreases. These elevated unsteady aerodynamic loads at high tilt angles are expected to influence rotor wake dynamics and acoustic radiation characteristics (discussed in Sections 5.2 and 5.3).

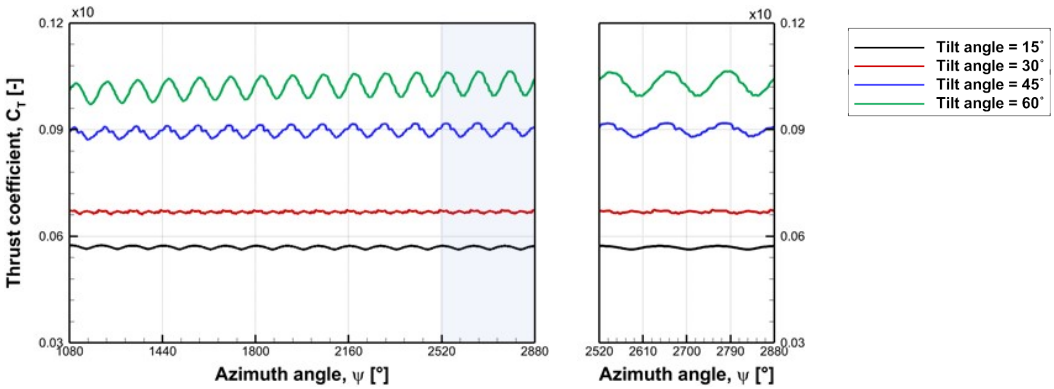

(a) (b)

Fig. 13. Time history of the thrust coefficient (C_T) for the rotor located on the starboard side under varying tilt angles: (a) over five rotor revolutions and (b) detailed view of one rotor revolution.

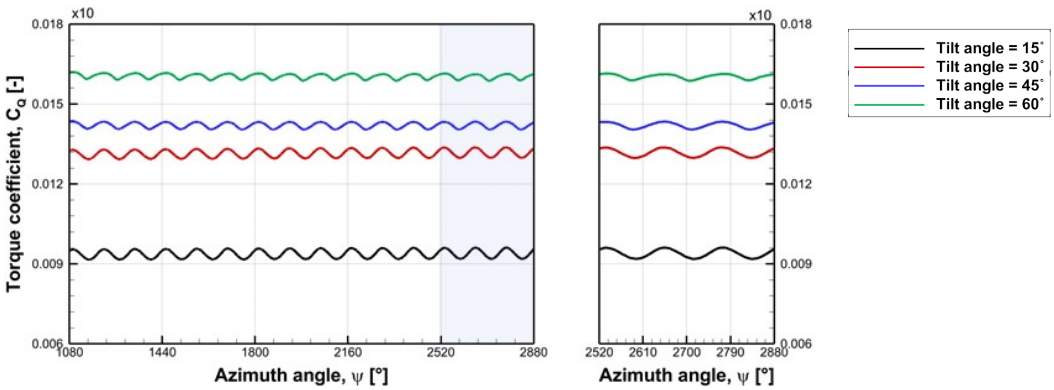

(a) (b)

Fig. 14. Time history of the torque coefficient (C_Q) for the rotor located on the starboard side under varying tilt angles: (a) over five rotor revolutions and (b) detailed view of one rotor revolution.

To further elucidate the impact of tilt angle on rotor aerodynamics, Fig. 15 depicts the azimuthal distribution of sectional C_T over the rotor disk over one complete rotor revolution. The contour plots are shown in the rotor reference frame, where $\psi_R = 0°$ corresponds to the aft side of the rotor (Fig. 11). At all tilt angles, the thrust distribution exhibits marked asymmetry, with consistently higher thrust loading on the advancing side of the

rotor disk (i.e., $\psi_R \approx 90°$). This asymmetry intensifies progressively as the tilt angle increases from 15° to 60°, which is attributable to variations in local inflow velocity across the rotor disk as the rotor tilts toward hover mode, forming distinct advancing and retreating sides of the rotor disk. The advancing side of the rotor disk experiences higher relative inflow velocities as the rotor tilts upward, producing greater lift and thrust. By contrast, its retreating side encounters reduced relative flow and lower aerodynamic loading. This imbalance generates an asymmetric distribution of the effective angle of attack, which is identified as the primary contributor to the increased peak-to-peak amplitude of aerodynamic loads with rising tilt angle, consistent with the results presented in Figs. 13 and 14. Furthermore, the contour plots indicate that the maximum thrust increases with increasing tilt angle, implying the generation of stronger tip vortices. The increasing difference in thrust between the advancing and retreating sides of the rotor disk amplifies asymmetry in rotor wake strength, indicating that the intensity of vortices shed from blade tips varies widely across the rotor disk, potentially increasing wake instability. Notably, the coexistence of tip vortices with varying strengths within the wake structure can intensify wake–wake interactions and promote early breakdown of the helical vortex system. A detailed investigation of the resulting wake characteristics and their dependence on tilt angle is presented in Section 5.2.

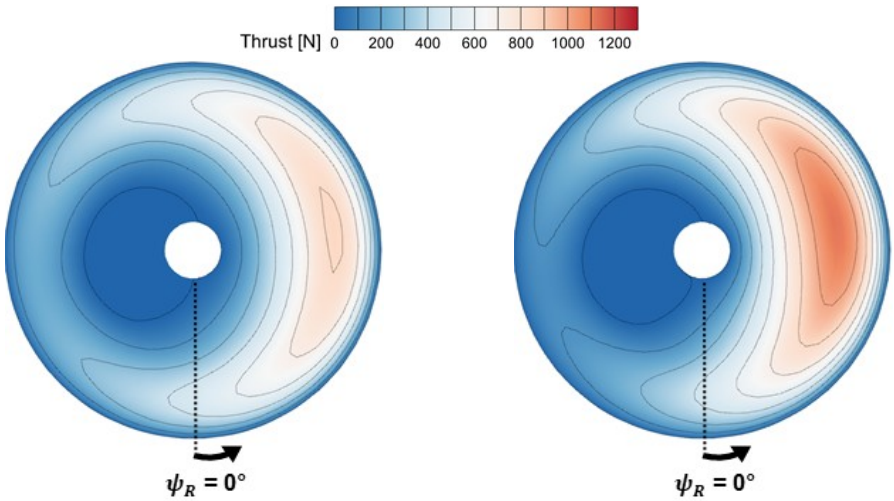

(a) (b)

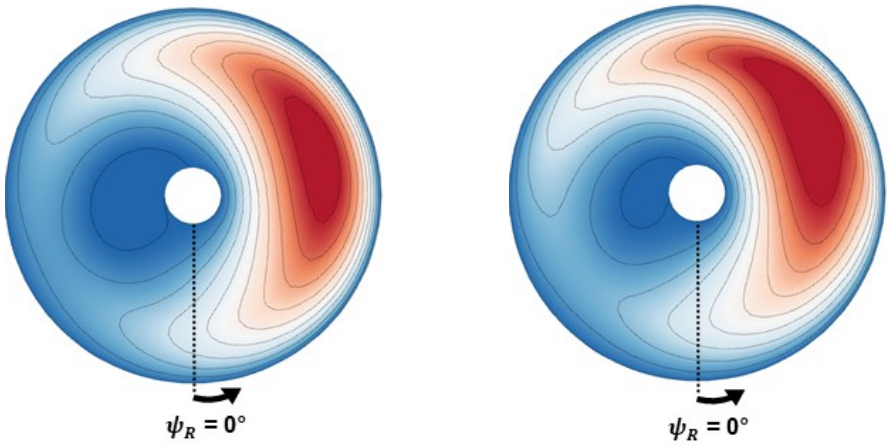

(c) (d)

Fig. 15. Contours of the sectional thrust coefficient (C_T) over the rotor disk under varying tilt angles: (a) 15°, (b) 30°, (c) 45°, and (d) 60°. ($\psi_R = 0°$ corresponds to the rear of the rotor).

Subsequently, the surface pressure distributions on the fuselage and main wing were analyzed to investigate the aerodynamic interference between the rotor and fuselage at varying tilt angles. Pressure data were extracted from four representative zones (Fig. 16): Zone A is aligned longitudinally along the upper fuselage surface, from the nose to a position near the horizontal stabilizer, while Zones B–D correspond to sections on the upper main-wing surface from inboard to outboard. The comparative results are presented in Fig. 17. For each tilt angle, the time-averaged pressure coefficients (denoted by solid lines) are plotted with standard deviation (denoted by error bars) to capture unsteady fluctuations associated with rotor wake impingement. A general trend is that the average surface pressure increases with increasing tilt angle in all zones. This behavior is attributable to the reduction in freestream velocity and associated dynamic pressure as the rotor transitions toward higher tilt angles. Zone A, located along the top of the fuselage and largely outside the direct influence of rotor downwash, exhibits smaller pressure variations compared to the wing sections, regardless of tilt angle. However, three prominent pressure peaks are observed near the nose, cockpit, and wing–fuselage junction, possibly induced by abrupt changes in fuselage curvature and associated pressure gradients in the Z-direction. By contrast, the wing sections (Zones B–D) display considerably greater sensitivity to tilt angle variations. Zone B, located near the inboard main wing region, experiences strong pressure fluctuations with increasing tilt angle. This can be attributed to the enhanced asymmetry in rotor aerodynamics, which becomes more pronounced with increasing tilt angle. Specifically, as the rotor tilts, the wake structure begins to break down, leading to large-scale vortex roll-up; further, the tip vortex trajectories exhibit substantial spatial disorder and coherence loss, with strong

radial contraction of the wake particularly evident near the azimuthal positions of 90° and 270°. These high-strength vortex structures dominate the wake dynamics near the inboard wing region. The intensified tip vortices convect closer toward the wing–fuselage junction as the rotor tilts, with the wake contracting radially inward, resulting in increased unsteady loading on the surface. Zone B is most susceptible to this tip vortex impingement, explaining the significant pressure fluctuations observed in this region. Meanwhile, the average pressure levels remain relatively consistent in Zones C and D, which are located farther outboard along the wingspan, although their fluctuations decrease with increasing tilt angle. The error bars in Fig. 17, representing the standard deviation of C_P values computed over five rotor revolutions, reflect the intensity of unsteady aerodynamic loading due to rotor–fuselage and rotor–wing interactions. Zones C and D demonstrate comparatively smaller fluctuations, particularly at higher tilt angles. The hub vortex generated from the retreating side of the rotor blade is the dominant unsteady flow feature in these regions. The aerodynamic asymmetry between the advancing and retreating sides of the rotor blade causes the vortex strength on the retreating side to diminish with increasing tilt angle, reducing its impact on surface pressure fluctuations. The reduced influence of the hub vortex at higher tilt angles explains the declining standard-deviation values observed in these outboard zones.

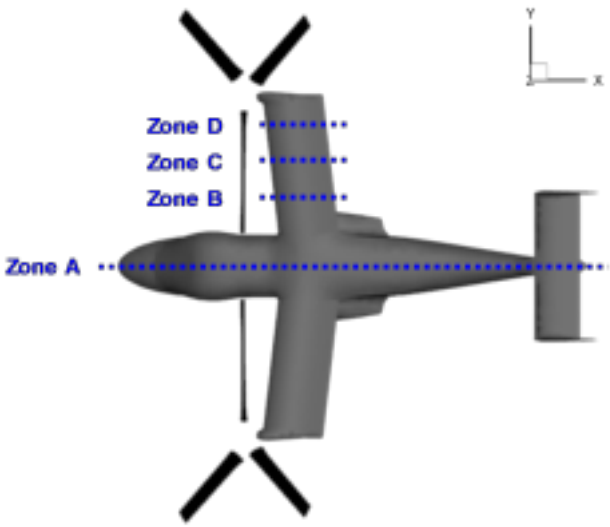

Fig. 16. Locations of surface pressure extraction on the fuselage (Zone A) and wing (Zones B–D) for evaluating rotor–airframe aerodynamic interactions under varying tilt angles.

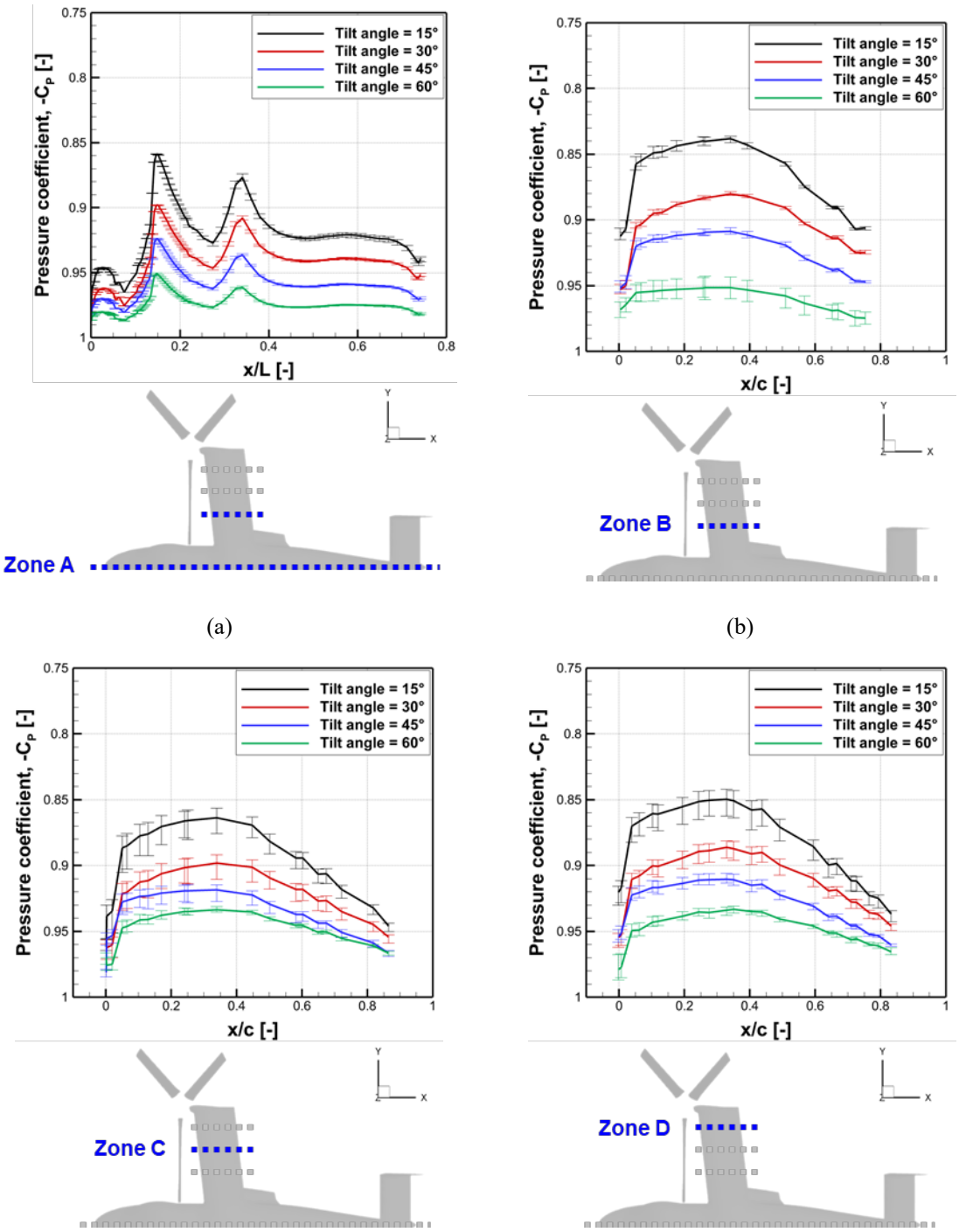

Fig. 17. Distribution of surface pressure coefficients (C_P) on the fuselage (Zone A) and wing (Zones B–D) under varying tilt angles. Solid lines indicate time-averaged values, and error bars represent the standard deviation across multiple rotor revolutions.

5.2 Effects of tilt angle on wake structures

Wake dynamics play a crucial role in determining rotorcraft aerodynamics and aeroacoustics, particularly for tiltrotor configurations in which the rotors operate in proximity to large airframe components such as wings and fuselage. The inflow experienced by the rotor becomes skewed as the rotor tilts during transition flight, wherein the freestream velocity is no longer aligned with the rotating plane. This skewed inflow modifies the evolution and coherence of the rotor wake, influencing wake–wake interactions and inducing wake instabilities.

Fig. 18 shows the predicted wake evolution in the X–Z plane at the four tilt angles, revealing that the tip vortices convect downstream from the rotor blades. The wake generated along the full span of the rotor blades was modeled using discrete Lagrangian vortex particles. The size and color of each vortex particle indicate its circulation strength, offering a qualitative representation of vortex intensity: particles with higher circulation, such as those forming strong tip vortices, appear as larger, red particles, whereas those with weaker vortices are represented by smaller, blue particles. The rotor wake exhibits a relatively stable and coherent helical structure at lower tilt angles of 15° and 30°, and the tip vortices convect downstream with minimal deformation, maintaining a consistent miss distance and alignment along the rotor thrust axis. The axial alignment of the freestream with the normal direction of the rotor disk allows the tip vortices to maintain a well-organized helical trajectory. The inflow distribution experienced by the rotor blades at low tilt angles remains symmetric relative to the azimuthal direction, yielding nearly uniform aerodynamic loads on the rotor blades. As previously discussed in the sectional thrust contour analysis (Fig. 15(a, b)), such inflow conditions result in reduced azimuthal variation in local blade loading and smaller peak-to-peak oscillations, leading to the development of coherent and well-organized helical wake structures.

However, the rotor experiences a more severe skewed inflow as the tilt angle increases to 45° and 60°, resulting in pronounced asymmetries in the strength and geometry of the wake structure. The skewed inflow relative to the rotor disk plane causes the formation of distinct upwind and downwind sides of the rotor. The upwind side corresponds to the azimuthal region in which the rotor blades encounter the freestream earlier in their rotational cycle; alternatively, the downwind side experiences the interaction later in the rotational cycle. This directional distinction gives rise to a deflected wake structure along the downwind side. Specifically, the upwind side ($\psi_R = 180°$) maintains a large separation between the shed vortices and rotor plane, resulting in a reduction in the induced velocity with upwash to the rotor blade and a higher effective angle of attack. This increase in the effective angle of attack on the downwind side of the rotor at higher tilt angles enhances thrust generation in the corresponding azimuthal region, as evidenced by the sectional thrust contours shown in Fig.

15(c, d). By contrast, the downwind side (ψ_R = 0°) exhibits reduced axial spacing between successive tip vortices, known as the wake pitch, with the tip vortices shed from blades located closer to the rotor plane. This proximity increases the magnitude of the induced velocity normal to the rotor disk, reducing the effective angle of attack and weakening local aerodynamic loading. With increasing tilt angle, the rotor wake becomes progressively deflected toward the downwind side owing to the increasingly skewed inflow. This deflection leads to greater disparity in the axial pitch distance of the wake between the upwind and downwind sides of the rotor and asymmetric aerodynamic loading across the rotor disk (Fig. 15(c, d)). Moreover, the wake structure becomes more skewed with increasing tilt angle, which in turn amplifies complex wake–wake interactions, promoting unsteady vortex dynamics such as vortex merging or reconnection. Consequently, the helical wake structure fails to coherently convect downstream and undergoes tip vortex breakdown at axial locations as early as $x / R \approx 2.5$, particularly at higher tilt angles (Fig. 18(d)).

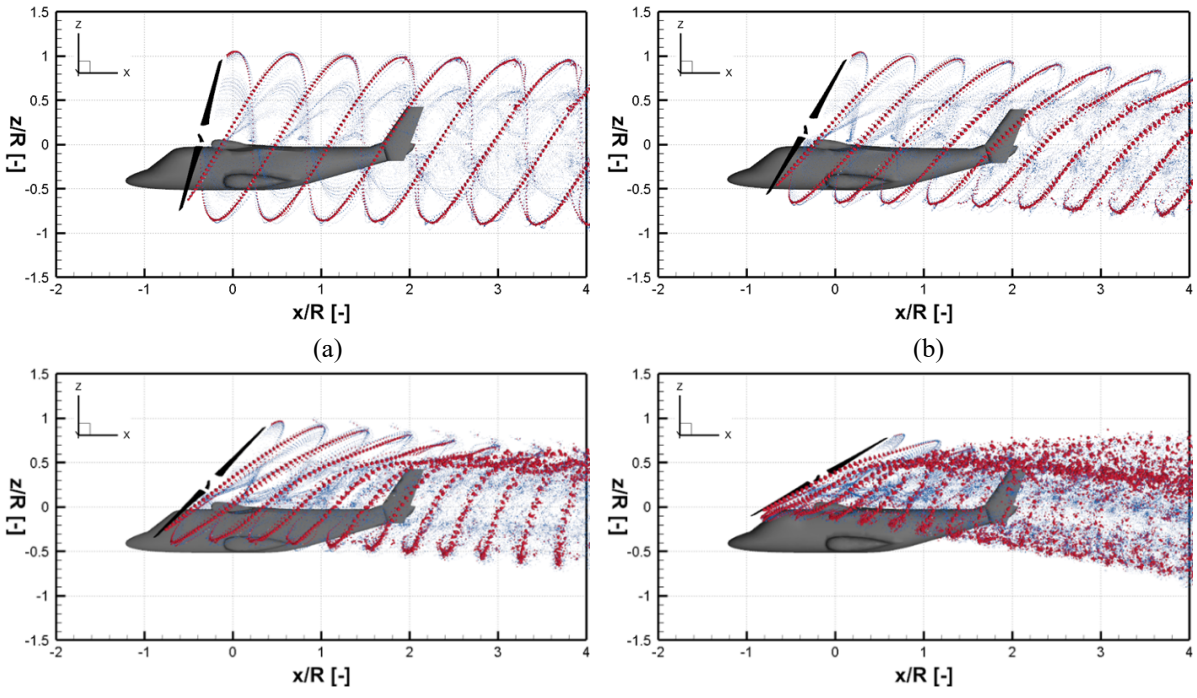

Fig. 18. Evolution of the rotor wake structure in the X–Z plane under different tilt angles: (a) 15°, (b) 30°, (c) 45°, and (d) 60°.

The preceding analysis in the X–Z plane highlighted the influence of tilt angle on the development of skewed wake structures, particularly the asymmetries between the upwind and downwind sides of the rotor; nevertheless, understanding the lateral wake evolution in the Y–Z plane and interactions with surrounding

airframe components is also critical. Figs. 19 and 20 present the wake structures in the Y–Z plane for the isolated rotor and full-configuration cases at representative tilt angles of 15° and 60°, respectively. The wake generated by the isolated rotor at a tilt angle of 15° (Fig. 19) exhibits a coherent and symmetric helical structure, with the tip vortices from the advancing and retreating sides of the rotor blade maintaining consistent strength. By contrast, minor local distortions emerge near the outer rotor disk region ($\psi_R = 270°$) in the wake generated by the full-configuration aircraft, with the rotor wake directly interacting with the wing and tail boom. This interaction causes minor deformations in tip vortex trajectory, although the overall wake coherence remains largely preserved. Rotor–fuselage interactions exert limited influence on wake evolution at lower tilt angles. However, the distinction between the wake structures generated by the isolated rotor and full-configuration aircraft becomes substantially more evident at a higher tilt angle (60°) (Fig. 20) and the wake deformation becomes considerably more pronounced, marking a clear contrast with the relatively stable behavior observed at 15°. The tip vortices exhibit marked radial contraction and azimuthal asymmetry in the wake generated by the isolated rotor, particularly near the advancing side of the rotor blade ($\psi_R \approx 90°$), where increased blade loading intensifies tip vortex strength. The intensified tip vortices on the advancing side of the rotor blade, combined with weakened vortex structures on the retreating side of the rotor blade, promote irregular interactions between adjacent wake particles. Conversely, substantial disruption is observed in the rotor wake generated by the full-configuration aircraft, especially in the inboard region near $\psi_R \approx 270°$, where direct interactions occur with the wing and empennage. These interactions trigger the rapid onset of tip vortex breakdown, characterized by a severe, early loss of coherent structure and earlier transition to a turbulent wake state. Consequently, wake interactional phenomena become pronounced at a tilt angle of 60° compared to lower tilt angles, primarily due to the lower forward speed of the rotorcraft and increased contact area between the rotor wake and fuselage. These results confirm that rotor–airframe interference in the Y–Z plane strongly depends on tilt angle and azimuthal position and that vortices on the retreating side of the rotor blade, particularly in the outboard region, are most susceptible to disruption.

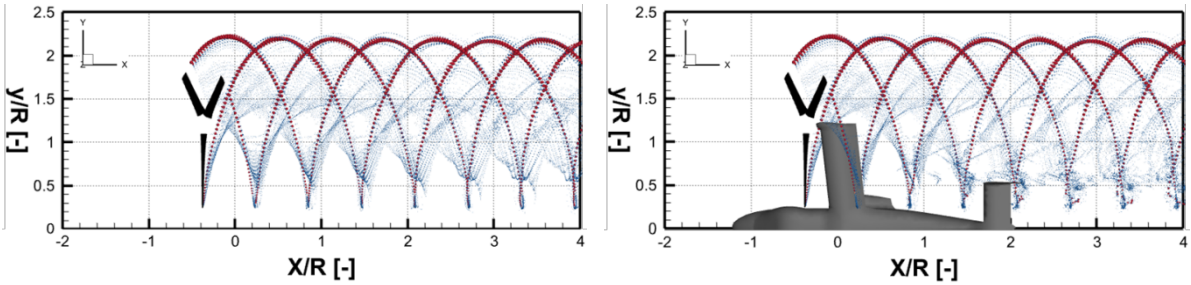

(a) (b)

Fig. 19. Comparison of wake structures in the Y–Z plane at a tilt angle of 15° for the (a) isolated rotor and (b) full-configuration aircraft.

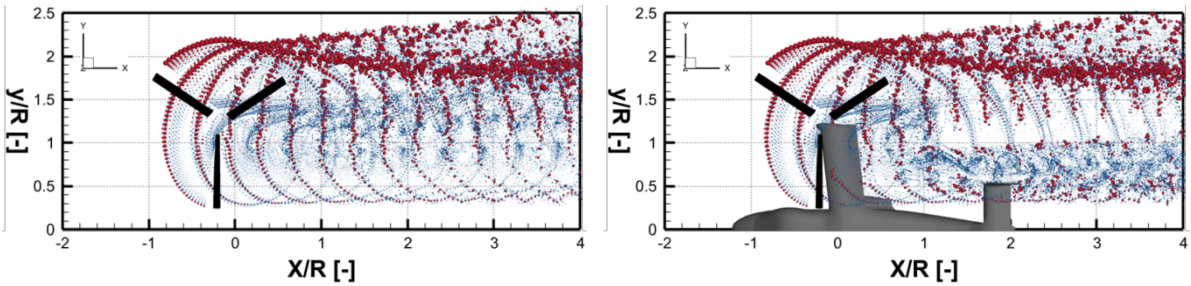

(a) (b)

Fig. 20. Comparison of wake structures in the Y–Z plane at a tilt angle of 60° for the (a) isolated rotor and (b) full-configuration aircraft.

As previously discussed, the unique geometric characteristics of tiltrotor aircraft inherently promote rotor–fuselage interactions that directly influence wake evolution, particularly at higher tilt angles. This section further elucidates the unsteady aerodynamic phenomena governing wake evolution by examining the streamwise vorticity field in the X–Y plane. Although prior analysis based on vortex particle trajectories highlighted the development of a skewed wake structure and azimuthal asymmetric characteristics, a vorticity-based approach offers a complementary Eulerian perspective on coherent structures such as tip vortices and their secondary interactions with the surrounding airframe. Notably, the strength and orientation of near-wake structures are essential for understanding aerodynamic loading and potential noise generation. Accordingly, the vorticity fields under varying tilt angles were compared to investigate the rotor–fuselage interference effects that govern near- and far-wake dynamics in full-configuration aircraft. The X-directed vorticity contours on the vertical cross section (X–Y plane) shown in Fig. 21 capture the wake field at the rotor mid-plane for tilt angles of 15°, 30°, 45°, and 60°. The color map distinguishes the direction and magnitude of local vorticity, with red and blue denoting opposite rotational directions. The observed wake features include shear layers and periodically shed tip vortices, forming well-defined vortex streets at lower tilt angles and gradually irregular and

diffuse vorticity fields at higher tilt angles. The vorticity field remains largely symmetric and periodic at a tilt angle of 15° (Fig. 21(a)), with evenly spaced counter-rotating vortex pairs convecting downstream. These coherent structures reflect balanced aerodynamic loading on the rotor blades and uniform inflow distribution. The tip vortices exhibit stronger circulation on the advancing side of the rotor blade, particularly near the outboard region of the wing, with minimal rotor–airframe interference, which is consistent with the organized wake structure presented in the vortex trajectory analysis (Figs. 18(b) and 19(b)). The coherence of the vorticity field is generally retained as the tilt angle increases to 30° (Fig. 21(b)), although the pitch of the vortex street decreases, indicating a shortened convection distance per rotor revolution compared to the case with a tilt angle of 15°. The tip vortex strength remains relatively symmetric; however, mild asymmetry in strength and spacing begins to emerge near the fuselage region. By contrast, the asymmetric vortical structure becomes evident at tilt angles of 45° and 60° as the rotor configuration approaches the hover mode. The wake becomes visibly more asymmetric and unsteady at a tilt angle of 45° (Fig. 21(c)). The advancing side of the rotor blade ($\psi_R \approx 90°$) produces stronger vorticity owing to higher blade loading, whereas the retreating side of the rotor blade ($\psi_R \approx 270°$) exhibits weaker vortical structure. Additionally, secondary vortices emerge downstream of the wing and tail regions, indicating considerable wake–wake interference. These effects are consistent with the onset of helical wake disruption and are closely tied to the increased skew angle and asymmetry in aerodynamic loading, as previously discussed. At the highest tilt angle of 60°, the vorticity field becomes highly unsteady and turbulent (Fig. 21(d)); this is particularly pronounced in the near-wake region, where strong rotor–fuselage interactions due to the tilted configuration coupled with severe wake–wake interactions arising from the highly skewed wake structure cause rapid coherence loss. The tip vortex trajectories lose coherence, with large-scale vortex roll-up developing near the fuselage and wing surfaces. The flow exhibits substantial spatial disorder, with abrupt loss of periodicity and strong radial-vorticity gradients, particularly downstream of the advancing side of each rotor blade. As shown in Figs. 18(d) and 20(b), full-configuration wake interactions result in early wake breakdown and transition into a turbulent wake state, indicating intensified rotor–fuselage interference and increased susceptibility to wake-induced loading and aeroacoustic effects.

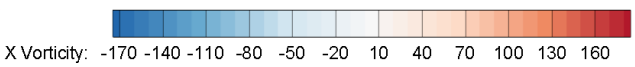

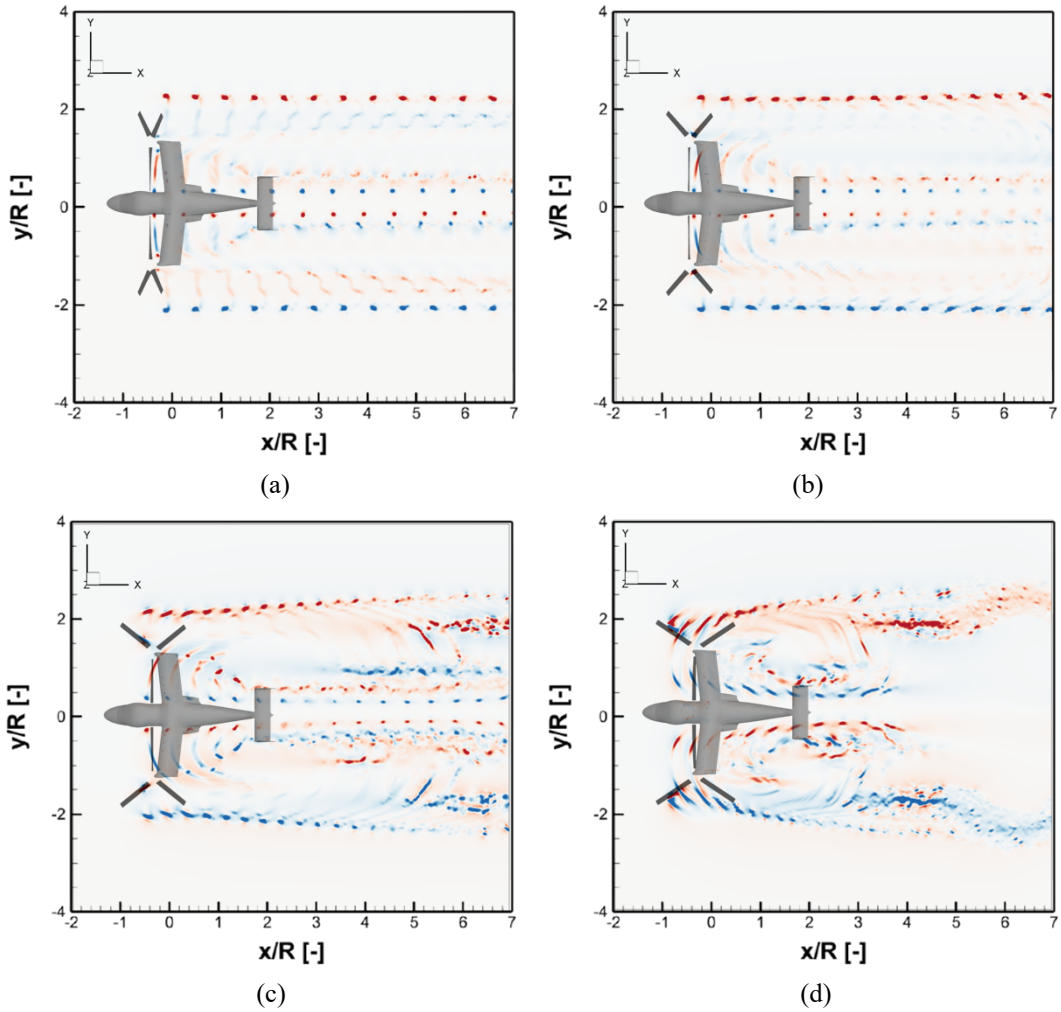

Fig. 21. Streamwise vorticity distribution (X-direction) visualized at the mid-height of the rotor disk in the X–Y plane under varying tilt angles: (a) 15°, (b) 30°, (c) 45°, and (d) 60°.

To further elucidate the wake dynamics of tiltrotor aircraft, the impact of the complex wake flow arising from interaction phenomena among the rotors, fuselage, and wings on the near-field velocity distribution around the main and tail wings was explored. As shown in Fig. 22, two representative cross sections (Zone A near the rotor plane and Zone B in the vicinity of the tail wing) were selected in the X–Z plane. These regions correspond to critical interaction regions where the wake encounters the main wing and tail surfaces. The instantaneous velocity fields at tilt angles of 15°, 30°, 45°, and 60° are presented in Fig. 23, where the left and right columns represent Zones A and B, respectively. Both zones exhibit well-defined tip vortex structures with symmetric axial velocity profiles at a low tilt angle of 15°. In Zone A, the induced flow concentrates in distinct regions corresponding to the advancing sides of each rotor disk, consistent with the helical wake geometry identified in earlier vorticity field analysis (Figs. 18(a) and 21(a)). Likewise, Zone B retains a relatively

undisturbed flow structure, indicating that the rotor wake convects downstream with minimal interference. The axial velocity distribution becomes progressively asymmetric as the tilt angle increases to 30° and 45°. In Zone A, the wake from the advancing side of the rotor blade intensifies and exhibits signs of contraction toward the rotor centerline. In Zone B, interaction between the skewed wake and tail region becomes more evident, as demonstrated by the deformation of velocity contours and the emergence of secondary flow regions. These effects are amplified at a tilt angle of 60°, where a strong concentration of axial velocity develops near the downwind side of the rotor owing to enhanced wake skewness and radial contraction. Moreover, tip vortices form on the advancing sides of the rotor blades at a tilt angle of 15°. However, at a tilt angle of 60°, a single high-intensity velocity core appears in both zones, corresponding to the merged strong-tip vortex roll-up on the advancing side of the rotor blade. This phenomenon is consistent with previous observations of intensified blade-loading asymmetry and wake breakdown (Figs. 15(d) and 18(d)). The near-field flow characteristics at higher tilt angles confirm that skewed inflow and rotor–fuselage interference disrupt helical wake structure evolution, introducing substantial axial flow nonuniformities near the fuselage and tail wing.

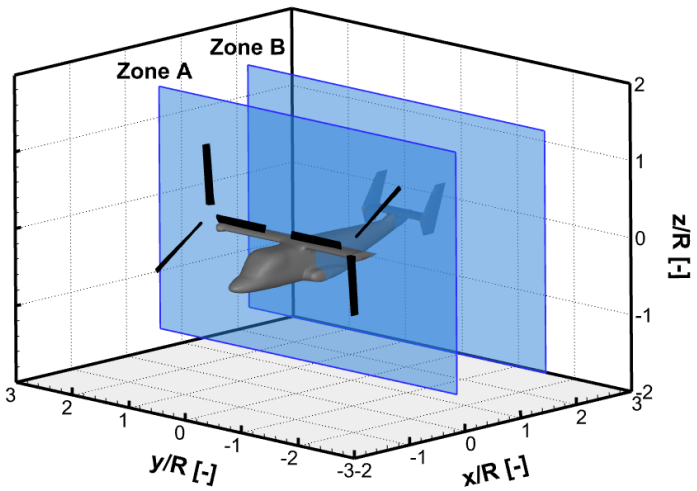

Fig. 22. Positions of X–Z sectional planes (Zones A and B) for analyzing near-field axial velocity distributions. Zones A and B are located near the rotor plane and near the tail wing, respectively.

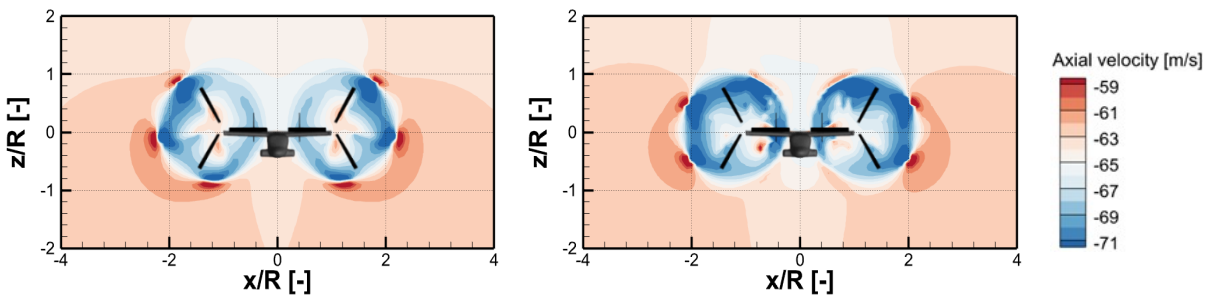

(a)

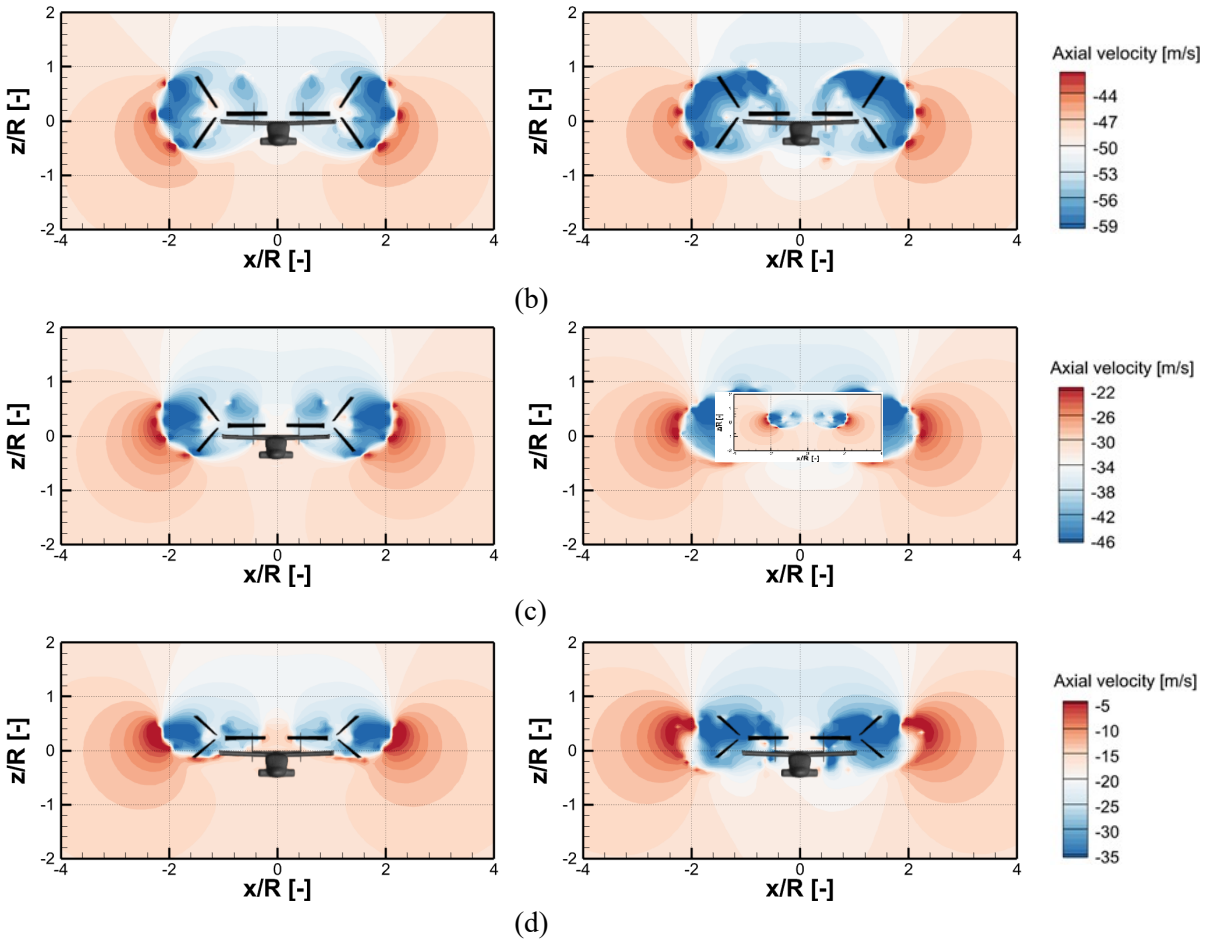

Fig. 23. Instantaneous contours of axial velocity (u_x) in Zone A (left) and Zone B (right) under varying tilt angles: (a) 15°, (b) 30°, (c) 45°, and (d) 60°. Contours highlight the evolution of wake-induced flow fields and the effects of rotor–fuselage interactions and wake asymmetry.

5.3 Effects of tilt angle on noise

In the present study, only thickness and loading noise components generated by the rotor blades were considered primary acoustic sources for the full-configuration tiltrotor aircraft. A planar microphone array comprising 600 virtual sensors was deployed 38.2 m (10R) below the aircraft to capture far-field noise radiation. The microphones were positioned in the forward (X) and lateral (Y) directions to enhance resolution near the expected peak radiation zones (see Fig. 10). The resulting OASPL fields for tilt angles of 15°, 30°, 45°, and 60° are presented in Fig. 24. The tiltrotor aircraft exhibits a symmetric noise radiation pattern at all tilt angles, with distinct noise lobes extending toward the starboard and port sides. These lateral noise lobes are clearly observed in Fig. 24, with intervening regions of lower SPLs. Notably, for all cases, the forward region of the aircraft consistently experiences higher noise levels than the aft region. The primary noise lobes shift forward with

increasing tilt angle, resulting in a corresponding displacement of the maximum-SPL location toward the front of the aircraft. Furthermore, a progressive increase in tilt angle is associated with an overall rise in SPL, indicating enhanced acoustic emissions. The noise radiation pattern exhibits a relatively symmetric distribution in the forward and downward directions at a low tilt angle (15°) (Fig. 24(a)), forming distinct noise lobes on either side of the longitudinal axis of aircraft. These patterns, which correspond to loading noise generated at the rotor disk, propagate dominantly in the direction normal to the disk plane. However, the directionality and intensity of the radiated noise undergo notable changes with increasing tilt angle. The noise lobes move forward and exhibit increased amplitude at tilt angles of 30° and 45° (Fig. 24(b, c)), with the peak SPL reaching 114.9 dB at a tilt angle of 45°, representing a 4 dB increase compared to that at a tilt angle of 15°. This rise in noise level is consistent with the increased rotor thrust and azimuthally nonuniform blade loading observed in the aerodynamic analysis, which contribute to stronger unsteady aerodynamic forces that are the primary source of loading noise. Additionally, the region of peak noise radiation shifts from near the aircraft to slightly ahead of it, highlighting a transition in dominant-noise-source orientation. Interestingly, although the tiltrotor generates the highest thrust at a tilt angle of 60° (Fig. 24(d)), the corresponding maximum SPL is slightly reduced to 114.5 dB, representing a 0.4 dB decrease compared that at a tilt angle of 45° (Fig. 24(c)). However, the region of low noise levels, visually indicated by the blue contours, substantially diminishes at a tilt angle of 60°. The increase in tilt angle results in more noise radiation despite a marginal reduction in peak acoustic output, which is primarily due to the increased unsteady aerodynamic loading caused by wake distortion and loss of tip vortex coherence at higher tilt angles, which enhances the loading-noise component in the acoustic field.

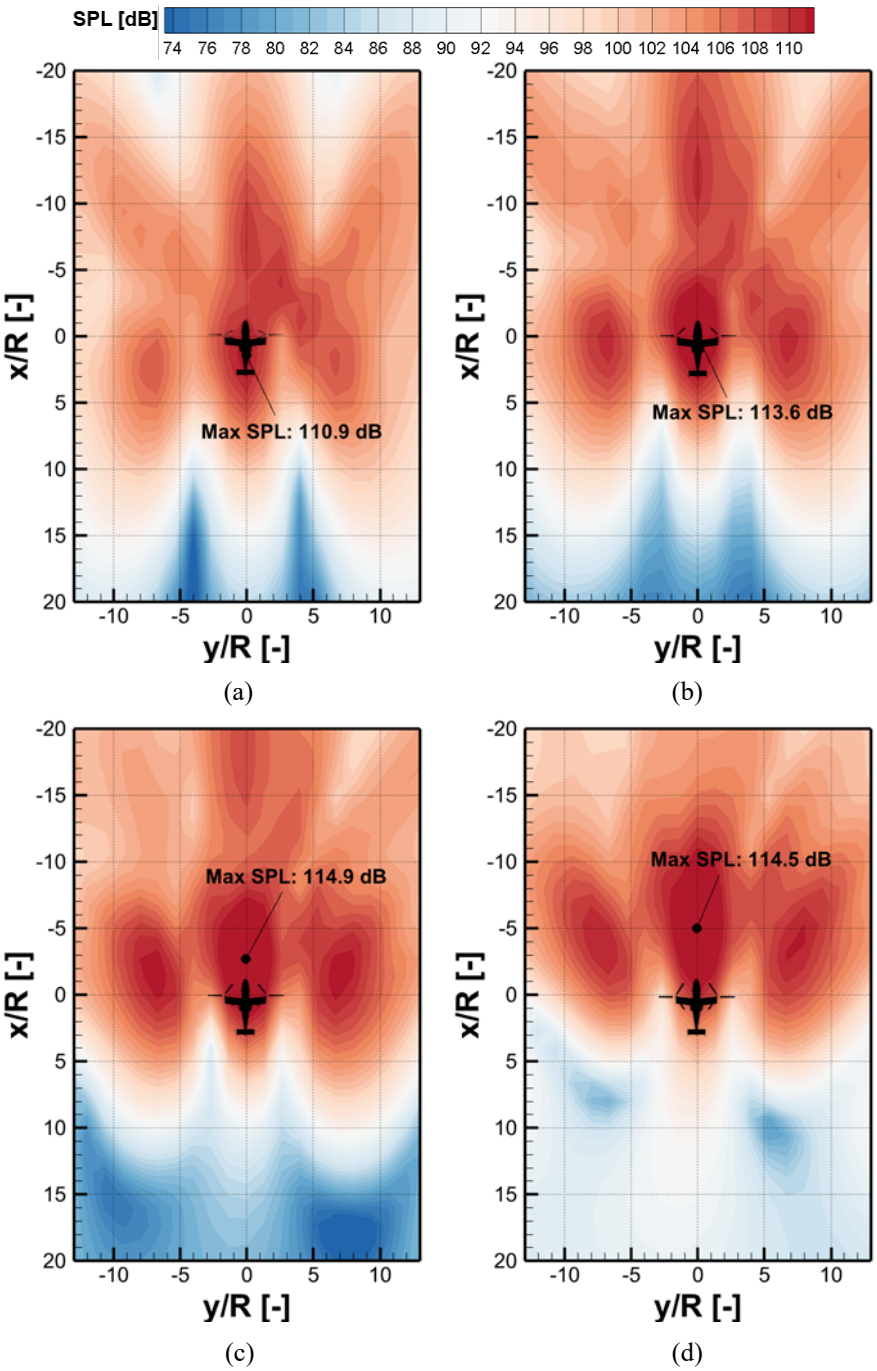

Fig. 24. Predicted distribution of SPL in the X–Y plane at 10R below the aircraft under varying tilt angles: (a) 15°, (b) 30°, (c) 45°, and (d) 60° (Maximum SPL values and their spatial locations are indicated.)

Fig. 25 compares the time-domain sound pressure signals decomposed into thickness and loading noise components at the microphone locations corresponding to the maximum SPL. The overall sound-pressure amplitude increases with increasing tilt angle, consistent with the trends observed in the OASPL noise map. The peak-to-peak amplitude of the total sound pressure closely matches that of loading noise at all tilt angles,

confirming that loading noise dominates the overall sound radiation. Alternatively, the contribution of thickness noise is nearly negligible at higher tilt angles. The total noise amplitude is reduced at tilt angles of 15° and 30° (Fig. 25(a, b)), corresponding to lower rotor thrust and reduced unsteady loading. Although the thickness noise contribution becomes more noticeable in these low-thrust cases, its magnitude remains too small to influence the OASPL trends. However, the sound pressure amplitude increases as the tilt angle increases to 45° and 60° (Fig. 25(c, d)) owing to increased aerodynamic loading and more pronounced unsteady blade forces. These results quantitatively confirm that loading noise is the primary source of noise radiation in the XV-15 tiltrotor during transition flight and that its amplitude depends on azimuthal variations in rotor aerodynamic loading.

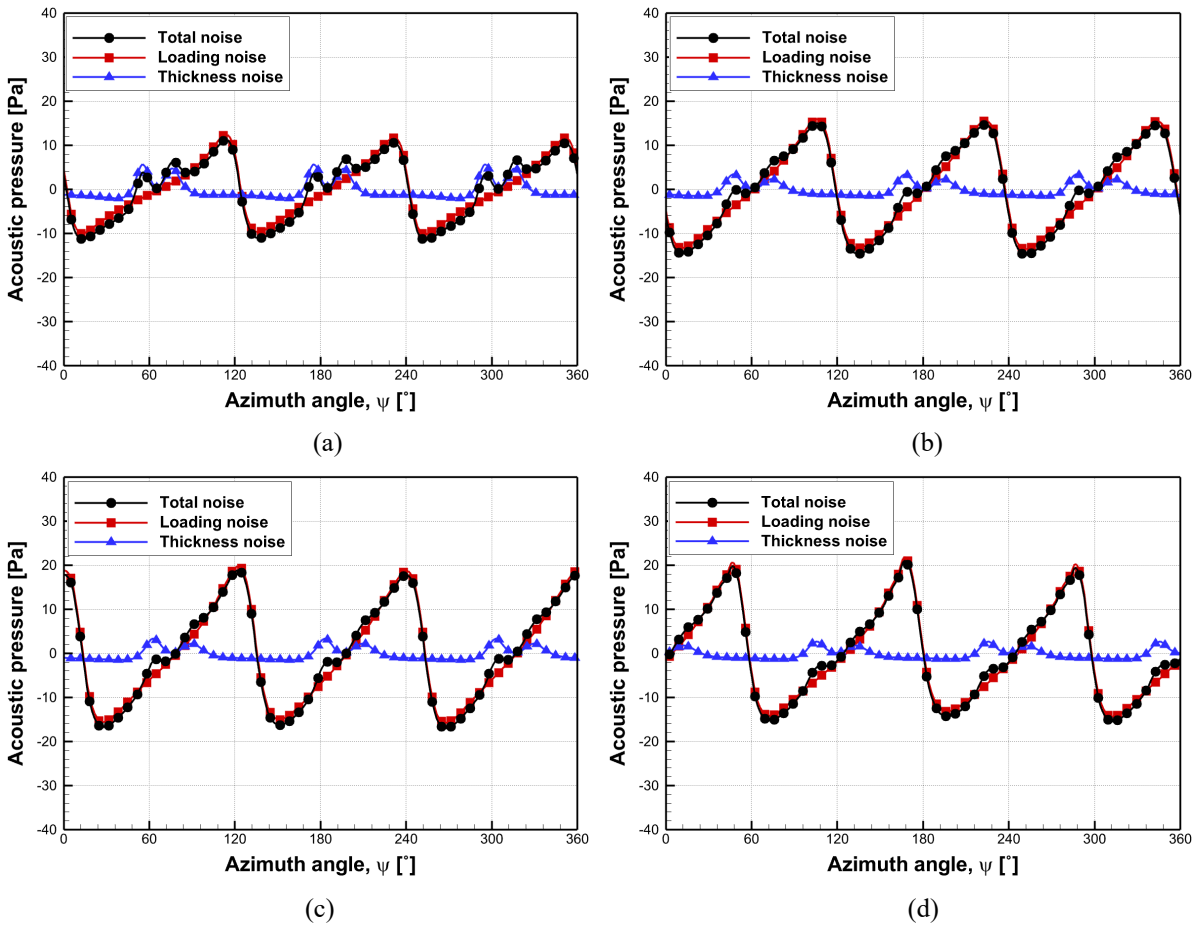

Fig. 25. Time-domain loading and thickness and total noise signals measured at microphone locations corresponding to maximum SPL under varying tilt angles: (a) 15°, (b) 30°, (c) 45°, and (d) 60°.

To further examine the unique characteristic of the noise lobes observed in the far-field acoustic maps (Fig. 24), time-domain loading-noise signals were analyzed at selected observer positions. As demonstrated in the preceding section, blade-loading noise constitutes the primary acoustic source for all considered tilt angles,

while thickness noise plays a secondary role. A detailed comparison was conducted for two representative tilt angles (15° and 60°), which exhibited a maximum SPL difference of ~4 dB. Two microphone positions were identified from the SPL contour maps for each tilt angle. One position corresponded to a region of minimum noise radiation within a lobe gap, representing an inter-lobe gap, while the other corresponded to the peak of a noise lobe. Specifically, microphone 1 (−14.8, −6.8, −10) and 2 (−9.3, −8.0, −10) was selected for the 15° tilt angle, and microphone 3 (−9.3, −5.2, −10) and 4 (−4.0, −6.8, −10) was used for the 60° tilt angle. All microphone locations were placed at a vertical offset of $z / R = -10$, corresponding to the measurement plane defined in the noise map. Fig. 26 presents the predicted time-domain sound pressure signals of the loading noise component at each microphone position, with the individual contributions from the left and right rotors superimposed onto the total signal. A comparison of the total sound-pressure signals, represented by the black solid lines with circular markers in Fig. 26, confirms that microphone 2 exhibits a higher sound-pressure amplitude than microphone 1 at a tilt angle of 15°. Similarly, microphone 4 exhibits a greater sound-pressure magnitude than microphone 3 at a tilt angle of 60°. These observations indicate that the acoustic signals from the left and right rotors exhibit clear phase differences at microphones 1 and 3, where minimum noise levels are observed in the SPL map. This out-of-phase condition causes partial destructive interference, reducing the amplitude of the combined sound-pressure signal. Such cancellation effects between rotor noise signals have also been reported in the forward region of multirotor configurations [24], further supporting the interpretation of the observed minima in the acoustic field. By contrast, at microphones 2 and 4, where SPL was maximized, the rotor contributions appear to be in phase, resulting in constructive interference and a higher overall sound-pressure magnitude. These findings reveal that the azimuthal phase relationship between the two rotors plays a critical role in shaping the far-field noise radiation pattern, particularly in the forward and downward directions. Despite the higher aerodynamic loading and rotor thrust at a tilt angle of 60°, the phase offset between acoustic signals radiating from the two rotor blades induced a cancellation effect at microphone 3, thereby lowering the effective SPL relative to the case of a tilt angle of 45°. This phenomenon underscores the critical influence of rotor–rotor phasing on the formation and modulation of loading noise in tiltrotor configurations during transition flight.

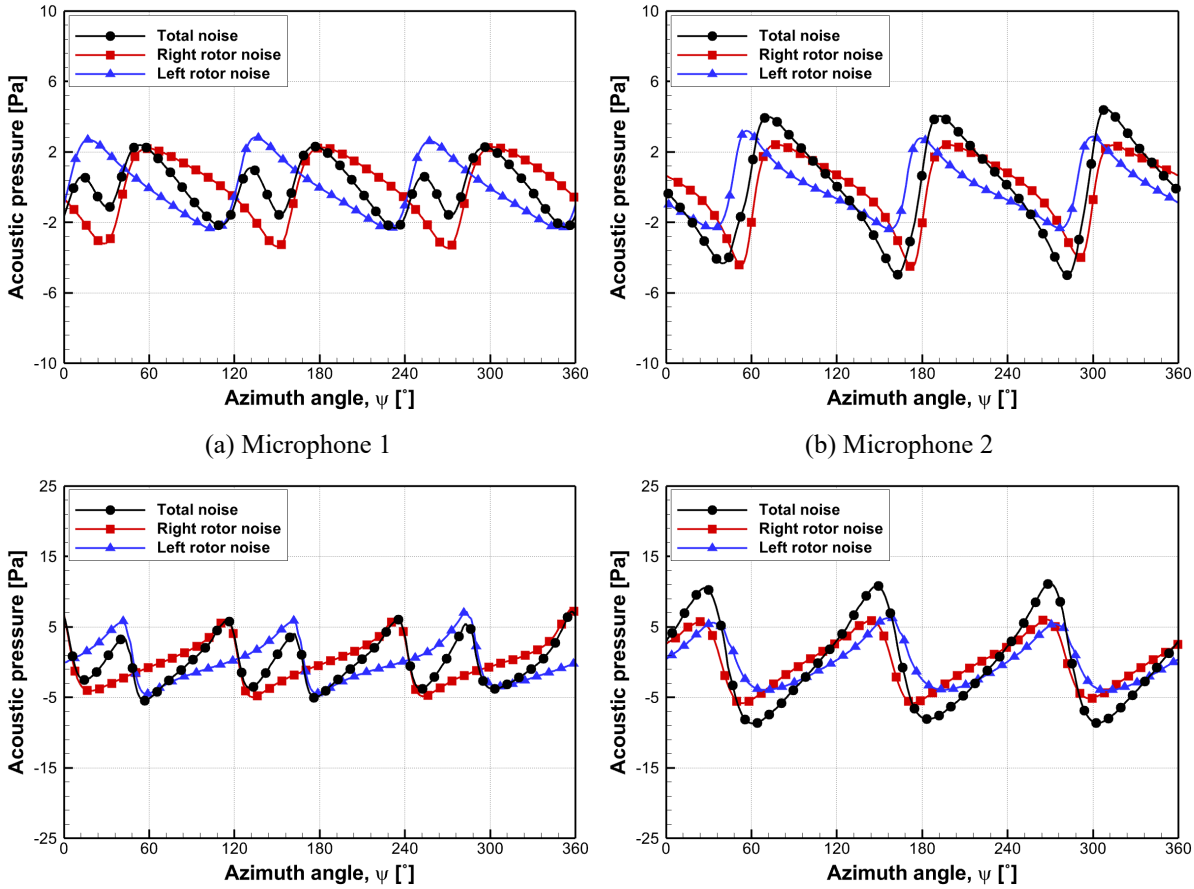

(a) Microphone 1 (b) Microphone 2

(c) Microphone 3 (d) Microphone 4

Fig. 26. Time-domain loading-noise signals measured at selected microphone locations for tilt angles of 15° and 60°. Each plot shows the total signal and contributions from the left and right rotors. Microphones 1 and 3 correspond to SPL minima in the acoustic field, while microphones 2 and 4 are located at SPL maxima.

6. Conclusions

This study numerically investigated the rotor aerodynamics, wake dynamics, and aeroacoustic characteristics of a full-configuration XV-15 tiltrotor aircraft during transition flight using a coupled-vortex method and Farassat's Formulation 1A. The influence of tilt angle on the aerodynamic loads acting on the rotor blades and fuselage, wake development, and noise radiation was explored, with a particular focus on rotor–airframe interaction effects. The key findings of the study are summarized below:

1. As the rotor transitions from airplane to helicopter mode, an increase in tilt angle intensifies loading on the rotor blades owing to a reduction in the inflow angle, resulting in a higher effective angle of attack and increased thrust and torque fluctuations. Furthermore, the skewed inflow introduces aerodynamic asymmetries between the advancing and retreating sides of the rotor blades, inducing 3/rev oscillations in thrust and torque performance.

2. The rotor wake retains a coherent helical structure at low tilt angles of 15° and 30°. However, wake skewness intensifies with increasing tilt angle, and wake–wake interactions and rotor–fuselage interference cause premature wake breakdown. The vorticity and velocity fields confirmed the presence of strong circulation gradients, large-scale vortex roll-up near the advancing side of the rotor, and severe disturbances induced by wing and tail interactions.
3. The magnitude of unsteady aerodynamic loading on the rotor blades intensifies with increasing tilt angle, resulting in elevated OASPL. The maximum-SPL location shifts forward with increasing tilt angle, with the SPL at 60° exceeding that at 15° by ~4 dB. Owing to the symmetry of the left and right rotors, the noise distribution in the lateral (port–starboard) direction remains largely symmetric. However, the noise radiation pattern becomes highly asymmetric in the forward and downward directions, creating strong directional noise lobes. Notably, phase differences between sound-pressure signals from the left and right rotors cause destructive or constructive interferences at certain microphone locations, influencing the spatial noise patterns observed in the SPL maps.

The findings of this study provide valuable insights into unsteady rotor aerodynamics, complex wake behavior, and the noise characteristics of the XV-15 tiltrotor aircraft under varying tilt angles. However, a limitation of this study is that the simulations assumed steady-state flight conditions at discrete tilt angles, preventing the capture of time-dependent transition dynamics. In addition, a major limitation of the current framework is the absence of a numerical trim routine capable of determining rotor blade pitch angles in real time. For unsteady flight, simulation parameters such as tilt angle, forward speed, and blade control inputs must vary dynamically; however, the present solver can only impose these variations on a predetermined schedule, without resolving pitch settings that satisfy the required rotor thrust or torque performance. To address this shortcoming, a trim routine is being developed to enable real-time computation of collective and cyclic pitch angles. These analyses will include implementing time-dependent tilt schedules and performing numerical trim analysis to account for transient aerodynamic responses and control effects during conversion flight. Nevertheless, the results of this study can serve as a foundation for advancing tiltrotor vehicle designs and operational guidelines to improve performance, safety, and acoustic comfort.

Declaration of competing for interest

The authors declare that they have no known competing financial interests or personal relationships that could have appeared to influence the work reported in this paper.

Acknowledgments

This study was supported by the National Research Foundation of Korea (NRF) grant funded by the Ministry of Science and ICT (Project Number: RS-2024-00397400 and RS-2025-25423496). This research was supported by 'regional innovation megaproject' program through the Korea Innovation Foundation funded by Ministry of Science and ICT (Project Number: RS-2023-IN231026). This work was supported by the Glocal University 30 Project Fund of Gyeongsang National University in 2025.

References

[1] D.J. Piatak, R.G. Kvaternik, M.W. Nixon, C.W. Langston, J.D. Singleton, R.L. Bennett, R.K. Brown, A wind-tunnel parametric investigation of tiltrotor whirl-flutter stability boundaries, in: America Helicopter Society 57th Annual Forum, Washington, DC, 2001.

[2] M. Maisel, D. Giulianetti, D. Dugan, The History of the XV-15 Tilt Rotor Research Aircraft from Concept to Flight, (2000).

[3] M.A. Potsdam, M.J. Silva, Tilt rotor aeromechanics phenomena in low speed flight, in: 2004 Users Group Conference (DOD_UGC'04), 2004: pp. 151–157. https://doi.org/10.1109/DOD_UGC.2004.46.

[4] D.-K. Kim, Technology trend on the future vertical lift (Rotorcraft), Current Industrial and Technological Trends in Aerospace 19 (2021) 51–61.

[5] P. Dunford, K. Lunn, R. Magnuson, R. Marr, The V-22 Osprey: a significant flight test challenge, (1990).

[6] R. Piccinini, M. Tugnoli, A. Zanotti, Numerical Investigation of the Rotor-Rotor Aerodynamic Interaction for eVTOL Aircraft Configurations, Energies (Basel) 13 (2020). https://doi.org/10.3390/en13225995.

[7] S. Tran, J. Lim, G. Nunez, A. Wissink, G. Bowen-Davies, CFD Calculations of the XV-15 Tiltrotor During Transition, 2019. https://doi.org/10.4050/F-0075-2019-14501.

[8] A. Zanotti, A. Velo, C. Pepe, A. Savino, D. Grassi, L. Riccobene, Aerodynamic interaction between tandem propellers in eVTOL transition flight configurations, Aerosp Sci Technol 147 (2024) 109017. https://doi.org/https://doi.org/10.1016/j.ast.2024.109017.

[9] N.S. Jamaluddin, A. Celik, K. Baskaran, D. Rezgui, M. Azarpeyvand, Aerodynamics and aeroacoustics characterisation of isolated rotor in hover and transition to forward flight, in: AIAA Aviation 2021 Forum, 2021: p. 2311.

[10] T. Ivanco, H. Kang, A. Kreshock, R. Thornburgh, B. Newman, Generalized Predictive Control for Active Stability Augmentation and Vibration Reduction on an Aeroelastic Tiltrotor Model, 2022. https://doi.org/10.2514/6.2022-0570.

[11] A. Zanotti, A. Savino, M. Palazzi, M. Tugnoli, V. Muscarello, MID-FIDELITY NUMERICAL APPROACH TO TILTROTOR AERODYNAMICS, 2021.

[12] A. Zanotti, A. Savino, M. Palazzi, M. Tugnoli, V. Muscarello, Assessment of a Mid-Fidelity Numerical Approach for the Investigation of Tiltrotor Aerodynamics, Applied Sciences 11 (2021) 3385. https://doi.org/10.3390/app11083385.

[13] A. Jimenez Garcia, G.N. Barakos, Numerical simulations on the ERICA tiltrotor, Aerosp Sci Technol 64 (2017) 171–191. https://doi.org/https://doi.org/10.1016/j.ast.2017.01.023.

[14] Z. Wu, C. Li, Y. Cao, Numerical Simulation of Rotor–Wing Transient Interaction for a Tiltrotor in the Transition Mode, Mathematics 7 (2019) 116. https://doi.org/10.3390/math7020116.

[15] G. Droandi, A. Zanotti, G. Gibertini, Aerodynamic Interaction between Rotor and Tilting Wing in Hovering Flight Condition, Journal of the American Helicopter Society 60 (2015). https://doi.org/10.4050/JAHS.60.042011.

[16] G. Droandi, G. Gibertini, D. Grassi, G. Campanardi, C. Liprino, Proprotor–wing aerodynamic interaction in the first stages of conversion from helicopter to aeroplane mode, Aerosp Sci Technol 58 (2016) 116–133. https://doi.org/https://doi.org/10.1016/j.ast.2016.08.013.

[17] F.F. Felker, J.S. Light, Aerodynamic interactions between a rotor and wing in hover, Journal of the American Helicopter Society 33 (1988) 53–61.

[18] J. Lim, Fundamental Investigation of Proprotor and Wing Interactions in Tiltrotor AIrcraft, 2021. https://doi.org/10.4050/F-0075-2019-14502.

[19] W. Appleton, A. Filippone, N. Bojdo, Interaction effects on the conversion corridor of tiltrotor aircraft, The Aeronautical Journal 125 (2021) 1–22. https://doi.org/10.1017/aer.2021.33.

[20] M. Tugnoli, D. Montagnani, M. Syal, G. Droandi, A. Zanotti, Mid-fidelity approach to aerodynamic simulations of unconventional VTOL aircraft configurations, Aerosp Sci Technol 115 (2021) 106804. https://doi.org/https://doi.org/10.1016/j.ast.2021.106804.

[21] B.D. Edwards, XV-15 tiltrotor aircraft noise characteristics, AHS (1990).

[22] D.A. Conner, M.A. Marcolini, B.D. Edwards, J.T. Brieger, XV-15 tiltrotor low noise terminal area operations, (1998).

[23] D.A. Conner, M.A. Marcolini, W.A. Decker, J.H. Cline, B.D. Edwards, C.O. Nicks, P.D. Klein, XV-15 tiltrotor low noise approach operations, in: American Helicopter Society 55th Annual Forum, 1999.

[24]W. Bao, W. Wang, X. Chen, H. Zhang, Q. Zhao, Numerical analyses of aeroacoustic characteristics of tiltrotor considering the aerodynamic interaction by the fuselage in hover, Aerosp Sci Technol 141 (2023) 108558. https://doi.org/https://doi.org/10.1016/j.ast.2023.108558.

[25]N.S. Jamaluddin, A. Celik, K. Baskaran, D. Rezgui, M. Azarpeyvand, Aerodynamic noise analysis of tilting rotor in edgewise flow conditions, J Sound Vib 582 (2024) 118423. https://doi.org/https://doi.org/10.1016/j.jsv.2024.118423.

[26]G.R. Coelho, J. Goldschmidt, H. Tingle, P. Ifju, L. Ukeiley, B. Goldman, M. Secchi, S.A.E. Miller, Aeroacoustic and Aerodynamic Interaction Effects Between EVTOL Rotors, (2023).

[27]J. Sagaga, S. Lee, High-fidelity computational study of aerodynamic noise of side-by-side rotor in full configuration, J Sound Vib 592 (2024) 118607. https://doi.org/10.1016/j.jsv.2024.118607.

[28]J. Sagaga, S. Lee, Performance, aerodynamics, and aeroacoustics of side-by-side rotors using high-fidelity computational fluid dynamics, AIAA Journal 61 (2023) 5429–5445.

[29]Z.H. Jia, S. Lee, High-fidelity computational analysis on the noise of a side-by-side hybrid VTOL aircraft, Journal of the American Helicopter Society 67 (2022) 1–14.

[30]Z.H. Jia, S. Lee, Computational study on noise of urban air mobility quadrotor aircraft, Journal of the American Helicopter Society 67 (2022) 1–15.

[31]B. Smith, U. Hebbar, D. Gandhi, The Effects of Rotor-Rotor and Rotor-Wing Interactions on eVTOL Aeroacoustics, 2023. https://doi.org/10.4050/F-0079-2023-17956.

[32]S. Kim, Y.-H. Hwang, R.S. Myong, H. Lee, Interactional aerodynamics and acoustics of a rotor with an airframe in hover, Physics of Fluids 36 (2024). https://doi.org/10.1063/5.0185036.

[33]M. Palazzi, Mid-Fidelity approach to tiltrotor aerodynamics, (2019).

[34]J. Katz, A. Plotkin, Low-speed aerodynamics, Cambridge university press, 2001.

[35]H. Lee, B. Sengupta, M.S. Araghizadeh, R.S. Myong, Review of vortex methods for rotor aerodynamics and wake dynamics, Advances in Aerodynamics 4 (2022) 20. https://doi.org/10.1186/s42774-022-00111-3.

[36]G.S. Winckelmans, A. Leonard, Contributions to Vortex Particle Methods for the Computation of Three-Dimensional Incompressible Unsteady Flows, J Comput Phys 109 (1993) 247–273. https://doi.org/https://doi.org/10.1006/jcph.1993.1216.

[37]H. Lee, D.-J. Lee, Numerical investigation of the aerodynamics and wake structures of horizontal axis wind turbines by using nonlinear vortex lattice method, Renew Energy 132 (2019) 1121–1133.

[38]H. Lee, D.-J. Lee, Wake impact on aerodynamic characteristics of horizontal axis wind turbine under yawed flow conditions, Renew Energy 136 (2019) 383–392.

[39]H. Lee, D.-J. Lee, Effects of platform motions on aerodynamic performance and unsteady wake evolution of a floating offshore wind turbine, Renew Energy 143 (2019) 9–23. https://doi.org/https://doi.org/10.1016/j.renene.2019.04.134.

[40]H. Lee, D.-J. Lee, Low Reynolds number effects on aerodynamic loads of a small scale wind turbine, Renew Energy 154 (2020) 1283–1293.

[41]W.-R. Kang, M. Park, H. Lee, Wake Behavior Analysis of Partial-Span Flaps Using Free-Wake Method with Gap Model, J Aircr 59 (2022) 1603–1607.

[42]H. Lee, D.-J. Lee, Rotor interactional effects on aerodynamic and noise characteristics of a small multirotor unmanned aerial vehicle, Physics of Fluids 32 (2020).

[43]B. Sengupta, Y. Lee, M.S. Araghizadeh, R.S. Myong, H. Lee, Comparative Analysis of Direct Method and Fast Multipole Method for Multirotor Wake Dynamics, International Journal of Aeronautical and Space Sciences 25 (2024) 789–808.

[44]B. Sengupta, E. Esmaeilifar, M. Sadegh Araghizadeh, S. Kang, H. Lee, R.S. Myong, L. Prince Raj, Rotor-Fuselage-Intake Aerodynamics and Icing Using Vortex and Eulerian–Lagrangian Computational Fluid Dynamics Methods, AIAA Journal (2025) 1–22.

[45]M.S. Araghizadeh, B. Sengupta, H. Lee, R.S. Myong, Aeroacoustic investigation of side-by-side urban air mobility aircraft in full configuration with ground effect, Physics of Fluids 36 (2024).

[46]M. Park, H. Lee, Acoustic Analogy with High-Order Time Derivatives for Far-Field Acoustic Predictions, Acoust Phys 69 (2023) 844–852.

[47]C.W. Acree Jr, R.J. Peyran, W. Johnson, Rotor design options for improving XV-15 Whirl-Flutter stability margins, 2004.

[48]U.K. Kaul, Effect of inflow boundary conditions on hovering tilt-rotor flows, in: Proceedings of the 7th International Conference on Computational Fluid Dynamics, ICCFD7, Big Island, Hawaii, 2012: pp. 1–19.

[49]J.M. Derlaga, C.W. Jackson, P.G. Buning, Recent progress in OVERFLOW convergence improvements, in: AIAA Scitech 2020 Forum, 2020: p. 1045.

[50]F.F. Felker, L.A. Young, D.B. Signor, Performance and loads data from a hover test of a full-scale advanced technology XV-15 rotor, 1986.

[51]A. Jimenez-Garcia, G.N. Barakos, S. Gates, Tiltrotor CFD Part I - validation, The Aeronautical Journal 121 (2017) 577–610. https://doi.org/DOI: 10.1017/aer.2017.17.

[52]B. Helicopter, Advancement of proprotor technology task. II: Wind-tunnel test results, NASA CR 114363 (1971).

[53]F. Jia, J. Moore, Q. Wang, Assessment of detached eddy simulation and sliding mesh interface in predicting tiltrotor performance in helicopter and airplane modes, in: AIAA Aviation 2021 Forum, 2021: p. 2601.

[54]C. Sheng, Q. Zhao, M. Hill, Investigations of XV-15 rotor hover performance and flow field using U2NCLE and HELIOS codes, in: 54th AIAA Aerospace Sciences Meeting, 2016: p. 303.

[55]J. Ma, Y. Lu, X. Xu, H. Yue, Research on near field aeroacoustics suppression of tilt-rotor aircraft based on rotor phase control, Applied Acoustics 186 (2022) 108451. https://doi.org/https://doi.org/10.1016/j.apacoust.2021.108451.

[56]R.E. Mineck, Steady and periodic pressure measurements on a generic helicopter fuselage model in the presence of a rotor, NASA, 2000.

[57]E.S. Bae, P. Rand, C. He, Hybrid Lagrangian-Eulerian approach for modeling aerodynamic interactions, in: AIAA Aviation 2019 Forum, 2019: p. 3474.

[58]C. Kitaplioglu, M. Betzina, W. Johnson, Blade-Vortex Interaction Noise of an Isolated Full-Scale XV-15 Tilt-Rotor, in: American Helicopter Society 56th Annual Forum Proceedings, Virginia Beach, VA, Citeseer, 2000.

[59]S.W. Ferguson, Development and validation of a simulation for a generic tilt-rotor aircraft, NASA CR 166537 (1989).